Modeling of Microvascular Shape Memory Composites.

By

John C. Terzak

Submitted in Partial Fulfillment of the Requirements

for the Degree of

Master of Science in Engineering

in the

Mechanical Engineering

Program

YOUNGSTOWN STATE UNIVERSITY

December, 2013

Modeling of Microvascular Shape Memory Composites

John C. Terzak

I hereby release this **thesis** to the public. I understand that this **thesis** will be made available from the OhioLINK ETD Center and the Maag Library Circulation Desk for public access. I also authorize the University or other individuals to make copies of this thesis as needed for scholarly research.

Signature:

John C. Terzak, Student Date

Approvals:

Dr. Pedro Cortes, Thesis Advisor Date

Dr. Hazel Marie, Committee Member Date

Dr. Daniel Suchora, Committee Member Date

Dr. Salvatore A. Sanders, Associate Dean of Graduate Studies Date

Abstract

This work investigates the adaptive and morphing properties of SMCs based on a shape memory polymer (SMP) and a microvascular arrangement of shape memory alloys (SMAs). Here, the microvascular SMA phase has been subjected to a two-way shape memory effect (SME) process, in order to fully control the actuation properties of the SMC. It has been observed that the two-way trained SMA successfully induces a morphing performance on the SMC during a fluid heating-cooling cycle. The initial results suggest that the actuation behavior of the SMC strongly depends on the microvascular fluid heating rate as well as on the temperature difference between the glass transition temperature of the SMP and the activation temperature of the SMA. Analytical and Finite Element Method (FEM) analysis on the microvascular SMC has also been performed. The results suggest that the FEA analysis offers a better prediction of the thermo-mechanical behavior of the SMC. It has been observed that whilst the FEA successfully predicts the thermal profile of the SMC, the mechanical modeling seems to require a degree of amendment. Here, the FEA has predicted a deflection 20% higher than those experimentally recorded. Although a refinement is needed on the mechanical modeling of the FEA analysis, the current FEA work certainly provides the elementary design parameters for future optimizations of morphing structures based on SMC.

Acknowledgements

My deepest and most sincere appreciation goes to the following people who have made this thesis possible.

Thesis Advisor

Dr. Pedro Cortes

Committee Members

Dr. Hazel Marie and Dr. Daniel Suchora

Faculty

Dr. Hyun Kim and Dr. Virgil Solomon

Additional Assistance

Dennis J Gajdos, STEM Computer System Administrator

Students

George Kubas and Travis Kneen

Wright Patterson AFRL/RXC Faculty

Jeff Baur and Dave Philips

Additional Thanks

NASA OSGC and Amber McClung, School of Engineering, Saint Mary University, San Antonio, TX.

Special Thanks

To my parents, for their support and always believing in me and enabling me to succeed in all that I choose to do.

Contents

Abstract ii
Acknowledgements iii
List of Figures vi
List of Tables xi
Nomenclature xii
1.0 Introduction 1
1.1 Shape Memory Alloys (SMAs) 2
1.2 Shape Memory Polymers (SMPs) 4
1.3 Shape Memory Composites (SMCs) 6
1.4 Motivation for Thesis 8
1.5 Objectives 8
1.6 Organization 9
1.7 Scope of Work 10
2.0 Literature Review 11
2.1 SMA 11
2.1.1 SMA Structural configuration 12
2.1.2 SMA Functional Properties. 17
2.1.3 SMA Applications 19
2.2 SMPs 22
2.2.1 SMP Functional Properties 22
2.2.2 SMP Applications 26
2.3 Modeling 28
2.3.1 SMA Modeling 28
2.3.2 SMP Modeling 32
2.3.3 SMC Modeling 33
3.0 Experimental Approach 36
3.1 Preliminary Experimentation 36
3.2 SMA Tubes 38
3.3 Microvascular SMC 39

4.0 Theoretical Modeling 42
4.1 Thermal Analysis 42
4.2 Mechanical Modeling 46
5.0 Finite Element Modeling 48
5.1 Model Geometry and Symmetry 48
5.2 Mesh 49
5.3 Fluid-Thermal Modeling 50
5.3.1 Determination of the Convection Coefficient, h, for ambiant environment. 51
5.4 SMA Modeling 52
5.4.1 SMA Fluid-Thermal Analysis 52
5.4.2 SMA Tube 53
5.5 SMC Coupled Thermo-Mechanical Modeling 54
5.5.1 SMC Transient Thermal Analysis 56
5.5.2 Coupled SMC 57
6.0 Results and Discussion 58
6.1 Experimental Results 58
6.1.1 Experimental Results: SMA 58
6.1.2 Experimental results: SMC 60
6.2 Theoretical Results 63
6.2.1 Theoretical Results of Plain SMA Tubes 63
6.2.2 Theoretical results: SMC 64
6.3 FEA Results 67
6.3.1 FEA Results: SMA 67
6.3.2 FEA results: SMC 69
6.4 Discussion 71
7.0 Conclusions 73
Bibliography 74
Appendix 78

List of Figures

Figure 1-1. Boeing SMART Rotor [2] 1

Figure 1-2. Chord-wise bending achieved by the heating of SMA strips in an antagonistic design. (a) Shape memory alloy adjustable camber (SMAAC) control surface internal actuator concept (b) Un-morphed (c) morphed. [4] 3

Figure 1-3. Inchworm-type robot for colon inspection [5]. 4

Figure 1-4. Deployable Structure Collapsed (Left) and deployed (right) [7] 5

Figure 1-5. Degradable shape-shape memory suture for wound closure. [9] 5

Figure 1-6. Morphing airfoil concepts a) folding wing concept where the SMP skin allows for wing morphing b) variable camber left)original (0 degree) right) Morphed configuration (15 degrees) [10] [11]. 6

Figure 1-7. Veritex (SMP-Carbon Fiber composite). [13]..... 7

Figure 2-1. Fabrication of Ni-Ti SMA. [15] 12

Figure 2-2 Pictoral representation of SMA's austenite and martensite crystallography [17]..... 13

Figure 2-3. Crystalline Transformations as a function of dislocation and temperature [18] 14

Figure 2-4. Structural change in common SMAs left) crystalline structure cycle. right) hysteresis profile [19]. 15

Figure 2-5. DSC test of Nitinol based SMA. The transition temperatures are identified by the inflection points in the graph. [20]..... 16

Figure 2-6. Structural characterization methods. (Left) Constant load test results. (Right) Active Af Test [21]..... 17
Figure 2-7. Comparison of OWSME and TWSME..... 18
Figure 2-8. Ni-Ti SMA Combined SE and SME, Temperature-Stress-Strain graphs [22]... 19
Figure 2-9. Application of SMAs as Exhaust Chevrons (Left) Static exhaust chevron. (Right) Active chevron assembly. [23]..... 19
Figure 2-10. Morphing airfoil concept (a) 15° in center using segments 5 & 6, (b) 10° using segments 7 & 8, (c) 10° using segments 3 & 4 and (d) 20° using all Segments (Linear Variation) [24]..... 21
Figure 2-11. SMA orthodontic wires. [25] 21
Figure 2-12. Elastomeric network through an SMP activation cycle. [28] 23
Figure 2-13. SMP activation cycle. 24
Figure 2-14. 3-D plot for SMP deformation as a function of temperature and applied force. [29] 25
Figure 2-15. Self-healing concept. (a) sample with crack prior to healing and (b) sample after self-healing [31]. 26
Figure 2-16. SMP suture going through stretching and re-heating process [9] 27
Figure 2-17. Model of SMP stent self-expanding in blood vessel. [33] 28
Figure 2-18. Matlab Simulink block diagram for predicting the actuation properties of SMA alloys with an electrical heating method of activation [39] 31
Figure 2-19. Tobushi's SMA-SMP Laminate belt Configuration. [40] 34

Figure 3-1. Manufactured Shape Memory Composite based on surface-embedded NiTi wires. Attached to the surface of the SMC is a strain gauge for measuring deflection. 37
Figure 3-2. TWSME on the SMA tube following a heating-cooling cycle using ethylene glycol as the thermal activation fluid. a) initial state b)fully active c) return to initial state after cooling. [48] 38
Figure 3-3. Micrograph of the manufactured microvascular SMC with a VfSMA = 2%. .. 40
Figure 3-4. Schematic of the heating-cooling pump system. The system shows a hot bath oil for heating the MEG during the activation process. [48] 41
Figure 4-1. Numerical mesh and Boundary Conditions. 45
Figure 4-2. Mechanical SMC loading case. 47
Figure 5-1. Model symmetries (left) SMA (Right) SMC. 49
Figure 5-2. SMC Mesh. 50
Figure 5-3. Boundary conditions for the SMA-fluid (shown for a quarter symmetry). 53
Figure 5-5. Mechanical Boundary Conditions on SMA. 54
Figure 5-4. Workbench project chart. 55
Figure 5-6. SMC Mechanical Boundary Conditions 57
Figure 6-1. Out of plane deflection angle of the SMA tube through the heating-cooling cycle. (left) initial starting angle, θ=0° in data (right) max angle achieved, θ=45°.... 59
Figure 6-2. Recorded actuation force as a function of temperature. 60

Figure 6-3. Observed deflection on the SMC through cycle (left) start of cycle (middle) max deflection, (right) end of cycle a) 2 tubes, max deflection ~ 10 mm. b) 3 tubes, max deflection ~13 mm. 61

Figure 6-4. Thermal results of the vascular SMC following a heating-cooling cycle a) SMC based on 3 tubes yielding a temperature of 73°C on the edge of the surface at the maximum out of plane deflection b) SMC based on2 tubes yielding a temperature of 69°C on the edge of the surface at the maximum out of plane deflection. 62

Figure 6-5 . Top view of SMC thermal results. (A) & (B) represent heating and cooling for the 2% $V_{f,SMA}$ (3 tubes) (C) & (D) represent heating and cooling for the 1.3% $V_{f,SMA}$ (2 tubes) 63

Figure 6-6. Effects of the percent volume of the SMA in SMC on its deflection. [49] 64

Figure 6-7. Minimum Temperature in SMP based on time. 65

Figure 6-8. SMA Thermal Results from FEA a) initial temperature, uniform profile b) t= 0.1 s, fluid thermal profile nearly developed, transient behavior along length c) t=1s, SMA temperature has no difference through its thickness, transient behavior on length d) after t=1s, uniform temperature, similar to that recorded by the fluid source. 68

Figure 6-9. FEA predicted deflection at end of SMA through heating and cooling cycle. [48] 69

Figure 6-10. Transient FEA thermal results. (Top) 3 tubes (2% $V_{f,SMA}$) , temperature on the edge at 240s: 66°C (Bottom) 2 tubes (2% $V_{f,SMA}$), minimum temperature of 56°C, at 240s. 70

Figure 6-11. Deviation of FEA from Experimental Results. Shown for 2% $V_{f,SMA}$ (3 tubes) 71

List of Tables

Table 2-1. Comparison of Austenite and Martensite Ni-Ti SMA. [15] 13

Table 2-2. Polystyrene based SMP mechanical properties. [30] 25

Table 3-1. Mechanical and thermal properties of the SMA and SMP. 37

Table 5-1. Ethylene Glycol Fluid Properties. 51

Table 5-2. Mechanical Properties. 56

Table 5-3. Thermal Properties. 56

Table 6-1. Out of plane deflection angle and force data as a function of temperature. . 59

Table 6-2. Time and temperature to reach steady state in the SMC. 66

Table 6-3. Deflection as a function of time (in mm). 67

Table 6-4. FEA Predicted deflection of the SMC located at the end of the SMP. 70

Table 6-5. Comparison of results. 72

Nomenclature

variable	description	units
x, y, z	spatial coordinates	mm
l, t, w	geometric values of thickness height and width, respectively	mm
A	Area	mm^2
V	Volume	mm^3
I	2^{nd} moment of inertia	mm^4
F	Force	N
σ	stress	MPa or GPa
ε	strain	mm/mm
δ	deflection	mm
E	Young's modulus	MPa or GPa
ν	poisson's ratio	unitless
α	thermal strain coefficient	mm/(mm*°C
T	Temperature	°C
h	convection coefficient	$W/(m^2*°C)$
k	conduction coefficient	W/(m*°C)
ρ	density	kg/m^3
μ	viscosity	kg/(m*s)
π	pi (3.14….)	unitless
α_T	thermal diffusivity	m^2/s
ξ	SMA martensite phase	unitless

1.0 Introduction

Smart Materials in the simplest terms are materials that can be trained to react to an external stimulus with a pre-established programmed structural shape response [1]. Their ability of being able to be trained for reacting in an established manner to thermal or electrical stimulus, could potentially lead to many advancements in smart-adaptive technology. This could result in the development of new structural designs in the transportation sector. Smart materials also could allow the incorporation of dynamic morphing structures in the aeronautic field, where the weight of the structures is a major design concern. One current example of morphing smart materials is the Boeing Smart Rotor [2], in which smart materials are utilized to greatly reduce vibrations.

Figure 1-1. Boeing SMART Rotor [2]

1.1 Shape Memory Alloys (SMAs)

Nowadays the most studied metal based smart material are the Shape Memory Alloys (SMAs), such as Ni-Ti (Nitinol), Cu-Al-Ni, Cu-Zn-Al and Au-Cd systems [3]. Each SMA system has its own unique characteristics that determine the ideal conditions for its use. Indeed, whereas iron based alloys are suitable for high temperature applications, Ni-Ti alloys are more appropriate for more moderate (up to 100°C) and room temperature applications. Although, SMAs have limited recovery strain features, they have large recovery stress properties which make them very useful materials for mechanical actuators [3]. Specifically, for applications in high pressure environments where their activation forces are needed to maintain a desired shape in addition to environmental forces [4]. One of the current technological developments that seems to demand the use of SMAs, is the concept of morphing wings in aircraft structures [4], where the SMA material will be used to maintain the shape of a smart airfoil while experiencing external lift and drag forces. Figure 2 shows the smart airfoil concept based on a SMA system.

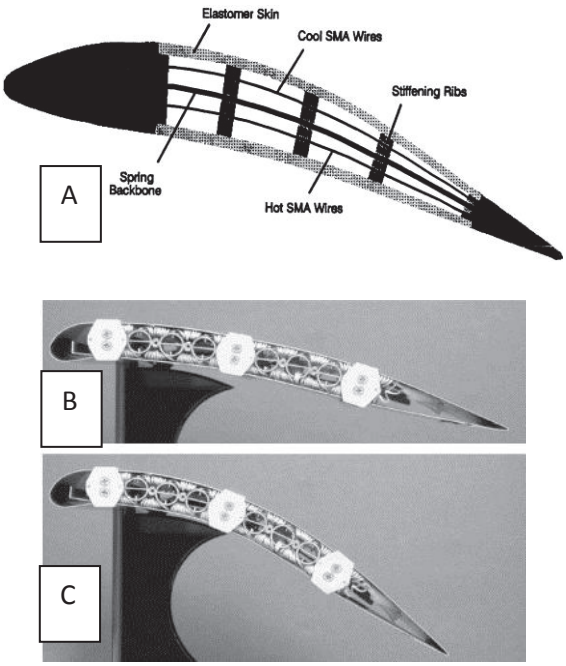

Figure 1-2. Chord-wise bending achieved by the heating of SMA strips in an antagonistic design. (a) Shape memory alloy adjustable camber (SMAAC) control surface internal actuator concept (b) Un-morphed (c) morphed. [4]

The medical field also has a number of applications that could potentially be revolutionized by the use of the SMA. Here, SMAs are being used in stints and gastro-intestinal intervention systems [5]. Figure 3 shows the exploratory Inchworm concept based on SMAs where its 3 sections, clamping, expanding and bending, act in a manner that allows for a large range of motion in studies of colon inspection. The ability for the actuation to be part of the material, allows it to be used on a micro scale approach.

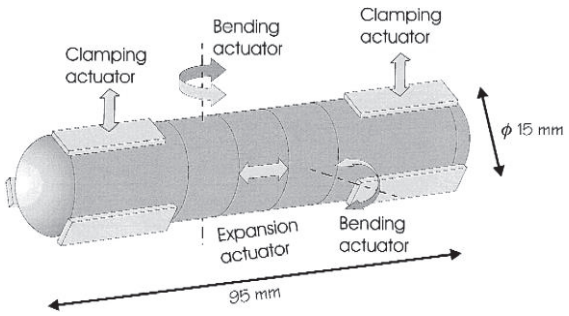

Figure 1-3. Inchworm-type robot for colon inspection [5].

1.2 Shape Memory Polymers (SMPs)

Another type of smart material that is rapidly emerging due to their light weight and high strain recovery capabilities is the Shape Memory Polymer (SMP). Unlike SMAs, SMPs have very large strain recovery properties but have limited stress recovery capabilities [6]. This makes them ideal for lightweight applications where large shape changes are required. SMPs seem to have a promising future in many applications, such as smart fabrics, heat-shrinkable tubes, films for electronics or for packaging, self-deployable sun sail structures for spacecraft, self-disassembling mobile phones, intelligent medical devices, and implants for minimally invasive surgery [6]. Figure 4shows a lightweight deployable structure based on SMPs, where the Smart Polymer can be stored in a relatively small space and subsequently thermally activated (deployed) to reach a desired size and shape [7].

Figure 1-4. Deployable Structure Collapsed (Left) and deployed (right) [7]

SMP are also being considered in the medical field [8]. Figure 1-5 shows a surgical suture utilizing SMP thread [9]. Here, the SMP shrinks as it is being heated, and closes the wound as a result. The biodegradable nature of the specific SMP used in this case allows for a single treatment of the wound. This feature adds convenience value for both the patient and the medical practitioner.

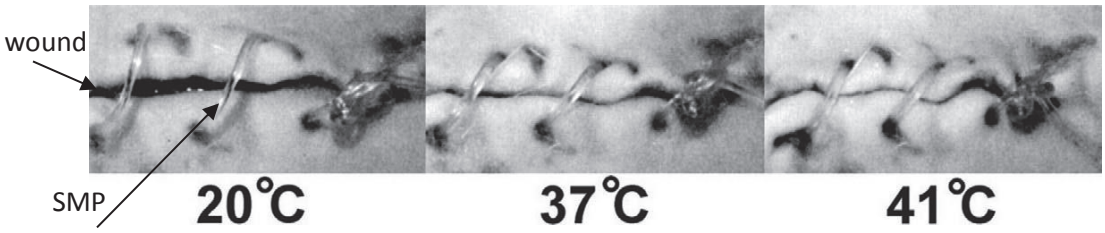

Figure 1-5. Degradable shape-shape memory suture for wound closure. [9]

SMPs also have the potential to be used in morphing wing designs. The folding wing concept allows for the wing to morph to a desired shape(see Figure 6). Here, the SMP serves as a stretching skin over the airfoil frame. This is a very attractive idea in the aeronautical industry because different types of aircraft structures have their own ideal wing configuration. An additional example of the use of SMP in the aerospace field is

the swept wing. The swept wing is meant to be used with different structural configurations during in-flight service with full extension during sharp turns to increase maneuverability [10]. Another attractive wing modification is the variable camber (see Figure 6b). Here, the ability for the variable camber allows for a wing to change configuration to vary its camber during the takeoff process. Then after takeoff, the camber can be reverted to in-flight configuration [11]. The lightweight of the SMP makes it a very lucrative option due to the fact that the SMP is significantly lighter than the materials currently used in the aerospace sector.

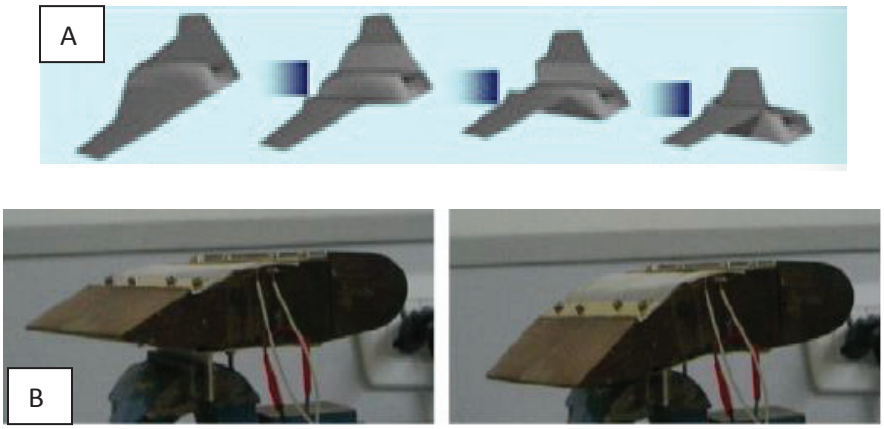

Figure 1-6. Morphing airfoil concepts a) folding wing concept where the SMP skin allows for wing morphing b) variable camber left)original (0 degree) right) Morphed configuration (15 degrees) [10] [11].

1.3 Shape Memory Composites (SMCs)

A composite is a material made from the combination of at least two materials with unique physical, chemical and mechanical properties [12]. In the engineering field plastics, metals, and ceramics are the most common constituents of composites. One of

the novel approaches in the area of composite structures is the incorporation of smart materials to generate actuating systems. Some of the initial attempts to create the smart composites have been addressed by CRG [13]. CRG currently manufactures Veritex, which is a carbon fiber reinforced SMP (see figure 7).

Figure 1-7. Veritex (SMP-Carbon Fiber composite). [13]

Further attempts at creating smart composites have spawned from several fields. The Aeronautic industry has discovered that the SMA or SMP alone may fall short of successfully achieving the desired design functionality of a morphing wing concept [10-11]. A composite system combining the high recovery strain and fixity capabilities of the SMP and the high recovery stress and actuation capability of SMAs may be a potential solution. This combination may also find uses in the biomedical field, specifically in the prosthetics area due to their ability to provide strength and flexibility. Smart composite systems based on SMAs and SMPs might also replace current physical actuators to lessen weight or overall design size. This opens up the use of hybrid smart

materials to an even larger pool of design possibilities making a FEA model advantageous for the quick assessment of a design's feasibility.

1.4 Motivation for Thesis

As mentioned before, there are many applications in the area of smart materials, such as the morphing wing concept where the sole use of SMA or SMP is not feasible. Either the SMA is simply too heavy to be used as the only material or the SMP doesn't have the cyclic actuation properties for morphing a structural component in flight conditions. This leads to the idea of investigating a composite that combines the high strain recovery and the fixity features of the SMP and the high recovery stress properties of the SMA for applications in morphing structures. Indeed, a model that can predict the actuation performance of SMCs represent a breakthrough in the area of morphing structures for spatial and time constraints. The proposed model could be used to predict optimal designs for specific applications with minimal weight and maximum actuation properties.

1.5 Objectives

There has been limited research carried out on the modeling frame of SMCs. The majority of what has been studied has been focused on a micro scale approach. The goal of the present research is to utilize an FEA and Engineering analysis to produce a transitional thermo-mechanical model for the design and optimization of an actuating SMC based on a microvascular network of thermally activated SMA tubes embedded in a SMP.

Goals

- Predict the actuation performance of plain SMA structures thermally activated for their use in smart composites as the actuator.
- Determine the transient thermal behavior of the SMA and SMP phases in the SMC.
- Determine the transient thermal distribution through the SMC.
- Investigate the inclusion of the thermal distribution of the system into a thermo-mechanical model following a heating and cooling process to determine the deflection.
- Validate results against experimental prototype.

1.6 Organization

This thesis will be presented in the following order:

A review containing a brief overview of shape memory materials is presented including the significance, purpose, and benefit of the present work. A review of the experimental research and theoretical modeling is also presented, followed by the experimental results and the modeling predictions. Finally the conclusions of this research program are presented.

1.7 Scope of Work

The approach taken to model the SMC has been comprised of two methods. The first being classical mechanics and fundamental theory. The theoretical analysis began with a static composite analysis. This static analysis determined whether the activation forces produced experimentally by the SMA were sufficient to produce the desired actuations in the composite based on temperature and percent of volume fraction in the SMC. An optimization of the percent of volume fraction of the SMA in the composite required to produce a morphing actuation was also investigated. Here, a theoretical transient heat transfer model was also applied to determine the temperature distribution through the composite as a function of time and spatial coordinates.

The second approach consisted of a Finite Element Analysis (FEA) using ANSYS FEA software. The FEA modeled the actuation performance of SMC through a transient thermal model. The investigated heat transfer model was used to produce the temperature distribution within the SMA and SMP and subsequently coupled with a mechanical model of the SMA to predict the thermo-mechanical behavior of the adaptive composite.

2.0 Literature Review

The literature Review will be presented in the following progression. First, the basic material functionality and applications will be discussed for SMAs and SMPs. This will be followed by an overview of the modeling efforts that have been carried out on each material individually. Lastly, a review of SMCs and the modeling efforts carried out on them will be presented.

2.1 SMA

A Shape Memory Alloy is a metallic material with the capability to morph its shape from a temporary configuration to its original shape under thermal stimulus. This capability stems from the Shape Memory Effect. The shape memory effect is the name for the ability of a material to remember its shape. The first observation of the Shape Memory Effect was on a pseudo-elastic Gold-Cadmium (Au-Cd) alloy in the 1930s. The Naval Ordinance Laboratory developed the first commercially available shape-memory material in the early 1960s [14]. These new shape memory materials were known as shape-memory alloys (SMAs) and were commercially marketed as Nitinol, a Nickel-Titanium alloy (Ni-Ti) [14]. The fabrication process of an SMA is shown in Figure 2-1. The importance of stoichiometry in the melting and casting phase is imperative, due to the fact that a 1% change in one constituent's content can result in 100K change in the transition temperature of the system [15].The Final and most important aspect of the fabrication of SMAs is the Shape Memory Treatment. Since it is where the SMA is trained with its desired Shape Memory Effect. The most common treatment method, is

known as ‘medium temperature treatment’ which consists of heating the SMA into a medium temperature range (350°C -450°C) while the SMA is fixed in its desired shape [16].

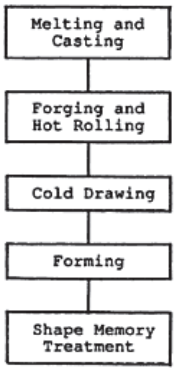

Figure 2-1. Fabrication of Ni-Ti SMA. [15]

2.1.1 SMA Structural configuration

Ni-Ti SMAs can exist in two different temperature dependent crystal structures called martensite and austenite. These phases are the source of the SMAs ability to ‘remember’ its shape. Due to the different crystal structures, the mechanical properties of austenite Ni-Ti are different than that shown by the same properties in martinsitic Ni-Ti (see table 2-1).

Table 2-1. Comparison of Austenite and Martensite Ni-Ti SMA. [15]

	Austenite	Martensite
Young's Modulus (GPa)	30-83	20-45
Ult. Tensile Strength (MPa)	800-1900	800-1900
% elongation at failure	20-25	20-25
% recoverable strain	8-10	8-10
Poisson Ratio	.33	.33

The crystallography of the SMA during their austenite phase is based on a body centered cubic structure (BCC), B-2, while the crystallography during martensite is less symmetric with a monoclinic B-19 arrangement. SMAs exhibit a transformation between a high temperature austenite phase, known as the parent phase and low-temperature B-19 monoclinic phase, which plays an important role in the associated shape memory effects. Additional treatments, such as cold working and thermal cycling can introduce an intermediate phase, known as rhombohedral phase, R phase (see figure 2-2).

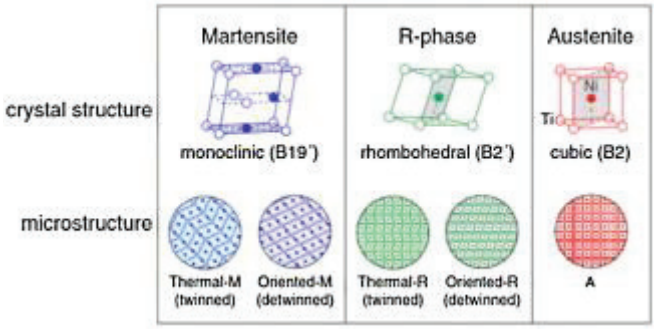

Figure 2-2 Pictoral representation of SMA's austenite and martensite crystallography [17].

The ability for the nickel titanium SMA to exhibit super elastic city and shape memory effect is based on the temperature-dependent austenite to martensite phase transformation at the atomic scale which is more commonly called the Thermo-elastic Martensite Transformation (TMT) [15].This transformation is a shear-like mechanism. If the temperature is raised, and the martensite becomes unstable, the reverse transformation occurs and the martensite phase reverts to the parent phase in the original orientation. The austenite to martensite phase transformation occurs in 2 mechanisms, the Bain strain and the lattice invariant strain. Basically, the Bain strain, also known as lattice deformation, consists of a series of atomic shifts between atoms, whereas the lattice invariant shear is possible via 2 mechanisms, slip and twinning. Slip is related to the dislocation process while twinning is associated to an instantaneous re-orientation of the crystal structure. Twin variants will easily move, and often times will condense into a single variant under stress, known as detwinning. The combined effect of Bain strain and twinning turns microscopic strain into a shear mechanism, the cycle is shown in figure 2-3.

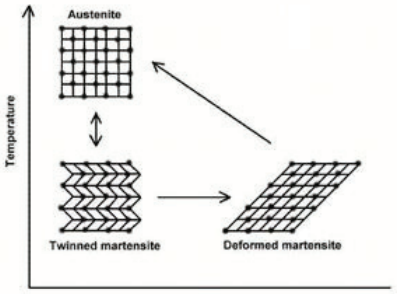

Figure 2-3. Crystalline Transformations as a function of dislocation and temperature [18]

The Transformation, however, has a hysteresis during the heating-cooling process. This hysteresis is classified by the martensite start and finish temperatures (M_s and M_f respectively) and austenite start and finish temperatures (A_s and A_f respectively) (see figure 2-4).These temperatures are characterized by the percent composition of Ni and Ti in the alloy. Figure 2-4 shows a side by side comparison of the crystalline structures along with the hysteretic behavior of a Ni-Ti SMA.

The four transformation temperatures of SMAs are commonly determined by a Differential Scanning Calorimetry (DSC). The DSC method determines the zero stress values of the transformation temperatures. A sample DSC for Ni-Ti SMA is shown in Figure 2-5. Here, the DSC detects crystallographic transitions as a function of the heat capacity in each structural transformation.

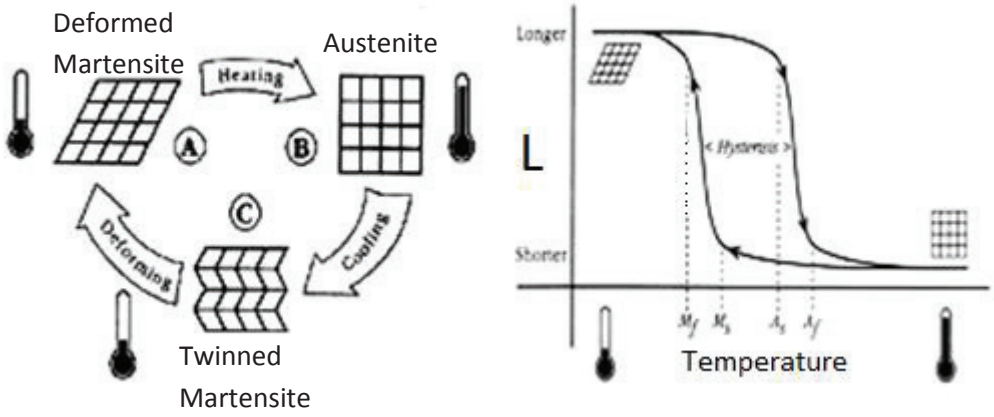

Figure 2-4. Structural change in common SMAs left) crystalline structure cycle. right) hysteresis profile [19].

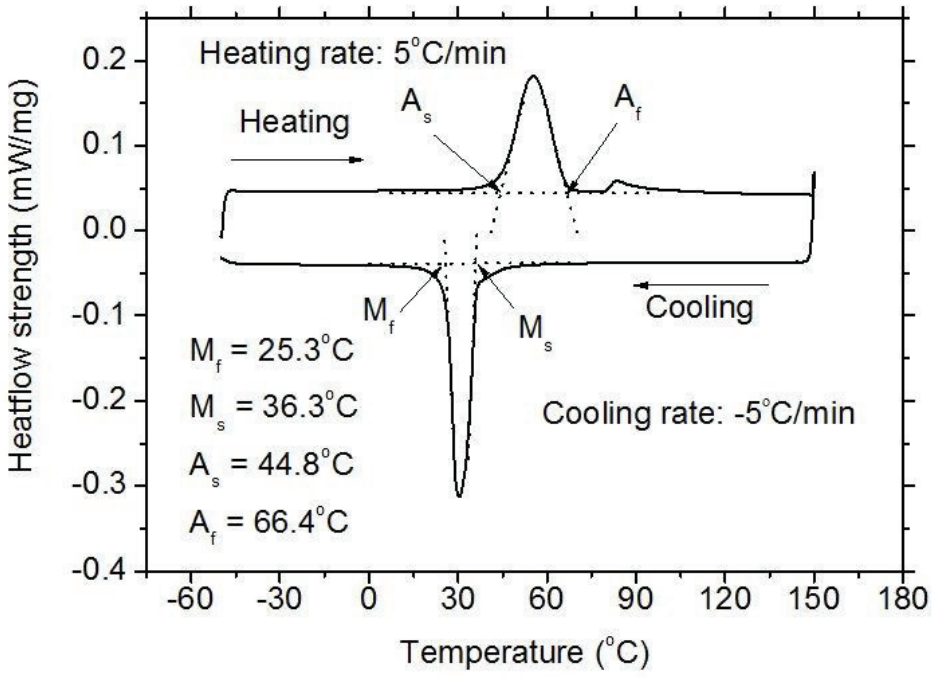

Figure 2-5. DSC test of Nitinol based SMA. The transition temperatures are identified by the inflection points in the graph. [20]

An additional method for determining the crystallographic changes in SMAs is the constant load method. In the constant load method, the specimen is loaded at a reference temperature, then heated and cooled while maintaining the constant load. The deformation is then recorded as a function of temperature. As shown in Figure 2-6 the Constant load test reveals the hysteresis and all the transformation temperatures. The Active Af method is another structural characterization method that is performed by bending the specimen while it is below its Martensite start temperature and slowly heating it while monitoring the shape. While crude, this method is consistent and very accurate. A representative Active Af test result is also shown in Figure 2-6.

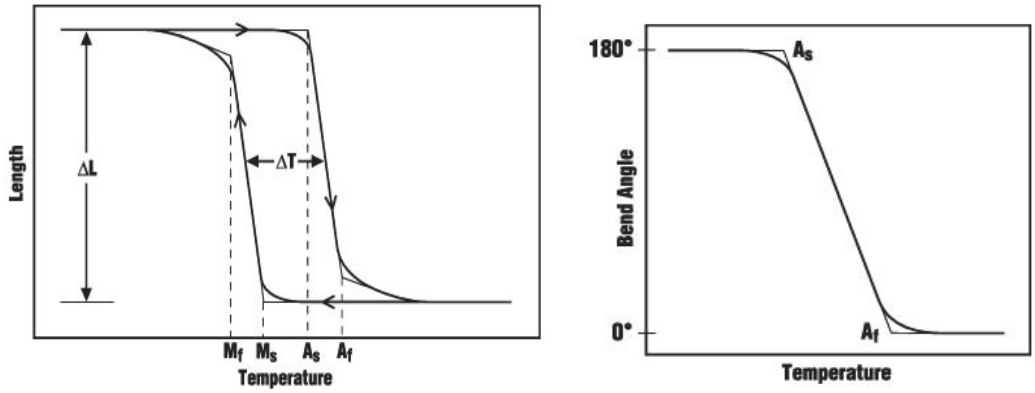

Figure 2-6. Structural characterization methods. (Left) Constant load test results. (Right) Active Af Test [21]

2.1.2 SMA Functional Properties.

The actuation properties, that SMAs exhibit, are known as the Shape Memory Effect (SME) and the Superelastic Effect (SE). The SME can exist in one or two way variants. With the One-Way SME (OWSME) the SMA only undergoes training to remember its austenite phase. The OWSME cycle begins with a physical deformation in the Martensite phase. Heating the SMA, results into the return to its parent Austenite shape. The SMA can subsequently be cooled, and the cycle can be repeated again. Two-Way SME (TWSME) training allows for the SMA to change shape upon heating and cooling, removing the need for an external force to be applied. A side by side comparison of OWSME and TWSME is shown in Figure 2-7. TWSME is commonly induced on SMAs by the dislocations created in the martensite phase under large deformations. This shape is trained by stressing the SMA below its M_f temperature or above its A_f temperature. Typically the training cycle is repeated to ensure its stability.

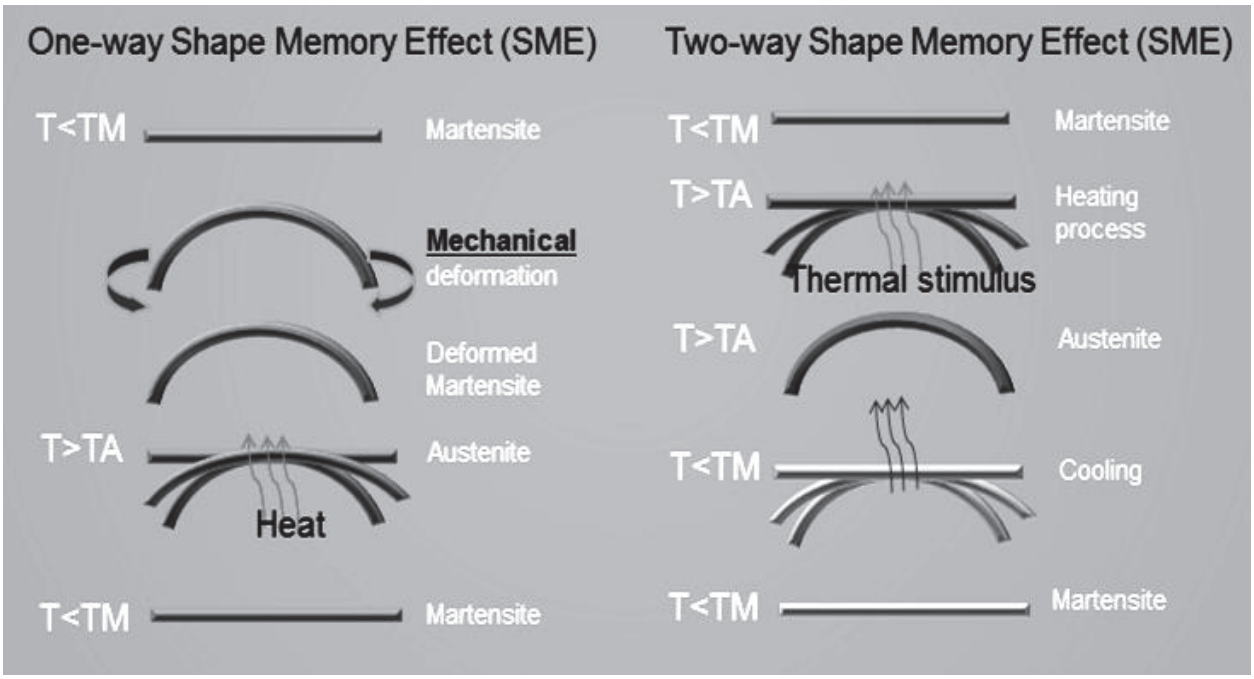

Figure 2-7. Comparison of OWSME and TWSME

The other active component of Ni-Ti SMAs is the Super-elastic Effect (SE), which is the recovery of deformation upon unloading. A representation of the SME and SE are shown in Figure 2-8. The combination of these two effects allows the SMA to undergo large deformations and high stress conditions repeatedly while still maintaining its functionality. It should be noted that the stress allowed by the SE far exceeds the stress within the SME. This fact accounts for the ability of the SMA to undergo the repeated SME cycles without yielding.

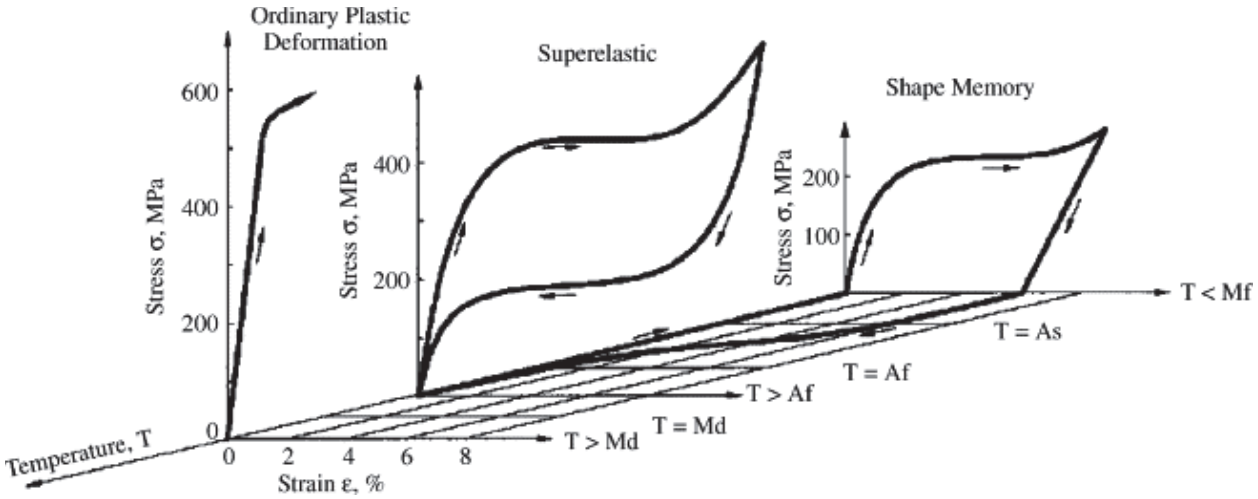

Figure 2-8. Ni-Ti SMA Combined SE and SME, Temperature-Stress-Strain graphs [22]

2.1.3 SMA Applications

The use of SMAs as actuators has been thoroughly explored in the aeronautical fields. SMAs have been used as Chevrons in jet turbine systems, and have shown a decrease in jet noise [4]. Also, active chevron systems using embedded SMA actuators, termed a SMA hybrid composite (SMAHC), have been parametrically studied for reducing noise during the takeoff and landing of airplanes [23]. An Exhaust chevron is shown in Figure 2-1.

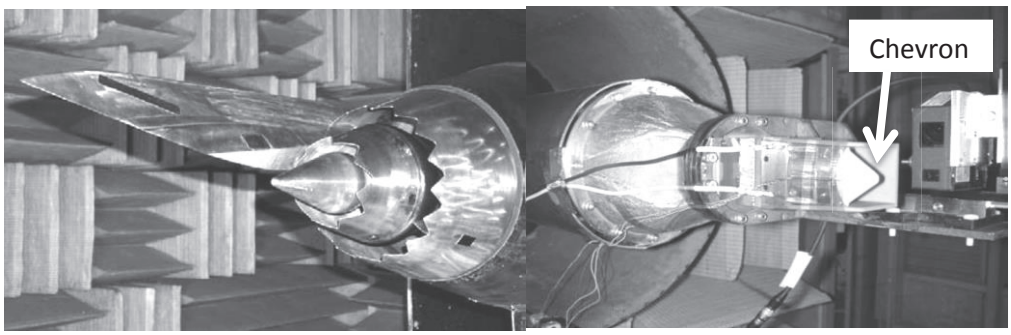

Figure 2-9. Application of SMAs as Exhaust Chevrons (Left) Static exhaust chevron. (Right) Active chevron assembly. [23]

One area of research and application that has received a great deal of attention is in the field of morphing aircraft structures (MASs), or morphing aircraft vehicles (MAVs). MAVs are single aircraft vehicles that are capable of changing structural shape in order to improve their performance over standard static design. The reasoning behind this advantage is that since current aircraft are designed with a wing geometry that offers optimal performance at one critical stage of flight (neglecting the other stages), morphing aircraft could offer optimal performance at multiple stages of flight [24].

A two-phase, eight-year MAVs program was funded by DARPA, NASA and AFRL in 2001 and resulted in a full-scale SMA-activated morphing aircraft able to utilize over 70 different wing shapes [24]. The wings contained 10 independent segments, each consisting of a honeycomb arrangement of SMA material covered by a silicon skin. Deflection rates of over 80 degrees per second and maximum deflections of over 20 degrees were achieved [24]. Figure 2-10shows some of the wing shapes that could be achieved in a morphing wing based on the aforementioned honeycomb SMA core material. The figure shows the maximum deflections of the morphing section of the wing.

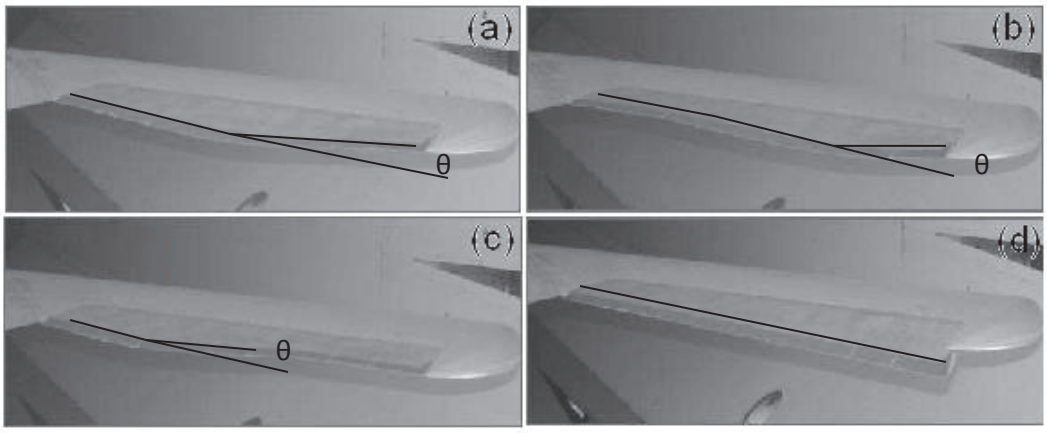

Figure 2-10. Morphing airfoil concept (a) 15° in center using segments 5 & 6, (b) 10° using segments 7 & 8, (c) 10° using segments 3 & 4 and (d) 20° using all Segments (Linear Variation) [24]

Additional applications of the SMAs have been in the medical field. Dr. Andreasen, from Iowa University, made the first implantation of an orthodontic device utilizing the pseudo elastic property of the Ni-Ti alloy (see Figure 2-11) [25].Ni-Ti wires, which are in austenitic phase at the temperature of the buccal cavity, provide constant force to reposition the teeth after being applied in the martensite phase. Other applications of SMAs in the biomedical field range from orthodontics to orthopedics, as well as in surgical pins and staples [26].

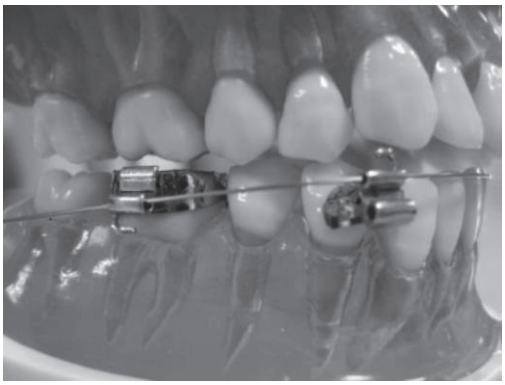

Figure 2-11. SMA orthodontic wires. [25]

2.2 SMPs

Shape Memory Polymers are an emerging smart material class. SMPs are an adaptive material that is able to be fixed into a temporary shape through the immobilization of their thermoplastic phase, typically through cooling. When heated above its glass transition temperature, an SMP will return to its originally shape due to its pre-existing elastomeric network already built within the structure. Simply put, the SMP 'remembers' its initial shape, and will return to it whenever it is activated. Shape-memory polymers were first introduced in 1984 by Nippon Zeon Co. in Japan [6]. These polynorborene-based SMPs had a limited glass temperature transition range as well as limited manufacturability. Mitsubishi Heavy Industry developed the first polyurethane-based SMP a few years later. Polyurethane-based SMPs are still the most widely used type of SMP [6].

2.2.1 SMP Functional Properties

Andreas Lendlein has completed three extensive literature reviews summarizing over 200 articles dealing with shape-memory polymer research ([6] [9] [27]). Topics reviewed include the many varieties in which SMP takes form, the physical and molecular mechanisms behind the shape-memory effect, the mechanical and thermal characteristics of SMPs and some of their current applications. An emerging class of SMPs that are activated by light have been the topic of discussion in Lendlein's more recent works [27], a large variety of applications could potentially benefit from the introduction of SMPs activated by light.

A graphic representation of the elastomeric network of the Shape Memory Effect on a SMP is shown in Figure 2-12 [28]. When the SMP is formed initially it forms the primary crosslinks that 'remember' its initial permanent shape. Heating the SMP above its glass transition temperature allows it to be mechanically deformed by an external force. Once a desired temporary shape is achieved cooling the SMP below its transition temperature will freeze the polymer in its current temporary shape creating secondary crosslinks. These secondary crosslinks are completely reversible. The external stimulus which formed the SMP to its temporary shape can be removed once the SMP is immobilized, since the secondary crosslinks hold the shape. Heating the SMP above its transition temperature without mechanical resistance will now cause the primary crosslinks to take over the shape of the SMP, reversing the secondary crosslinks and reforming the original shape.

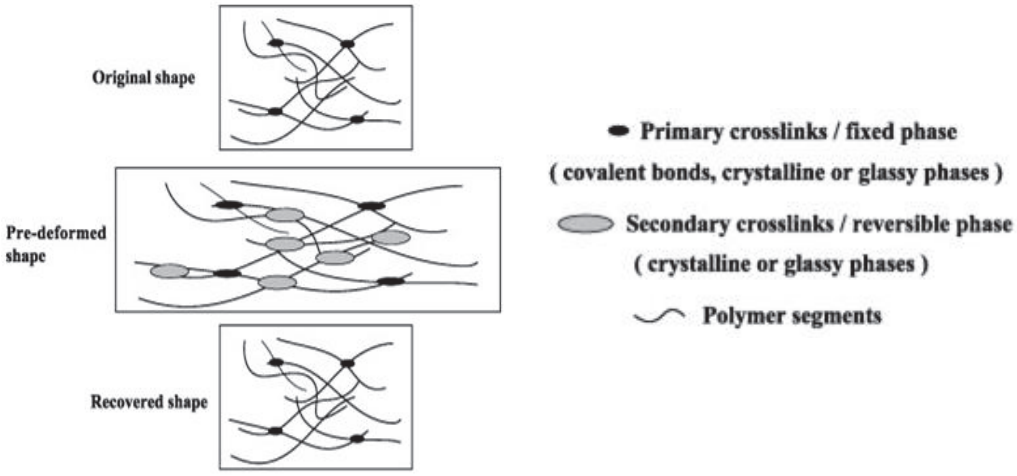

Figure 2-12. Elastomeric network through an SMP activation cycle. [28]

A macroscopic view, like the one shown in Figure 2-13, of the SMP's Shape Memory cycle is helpful to pair with the previously discussed elastomeric network

pictorial. The SMP is heated above its T_g and a force is applied to generating the deformed shape. The SMP is then cooled below its T_g while the force is maintained. Once below the T_g, the force may be removed and the SMP will hold its deformed shape. Heating the SMP now will activate its recovery of the permanent shape.

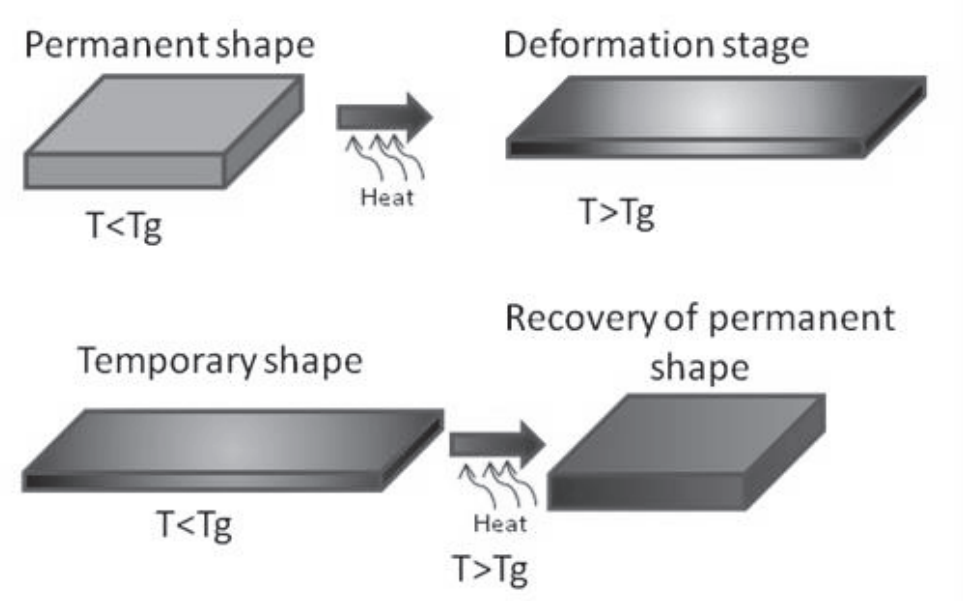

Figure 2-13. SMP activation cycle.

SMPs exhibit SE and SME and currently exist only in an equivalent to the one way trained SMAs because they only have the capability to 'remember' one shape (their parent shape). SMP deform as a function of both temperature and applied force, as shown in figure 2-14 [29]. It can be seen in the figure 2-7 that until the SMP is heated above its T_g, it resists all deformation on what is called its glassy state. Once heated, the SMP is considered rubbery and allows deflection.

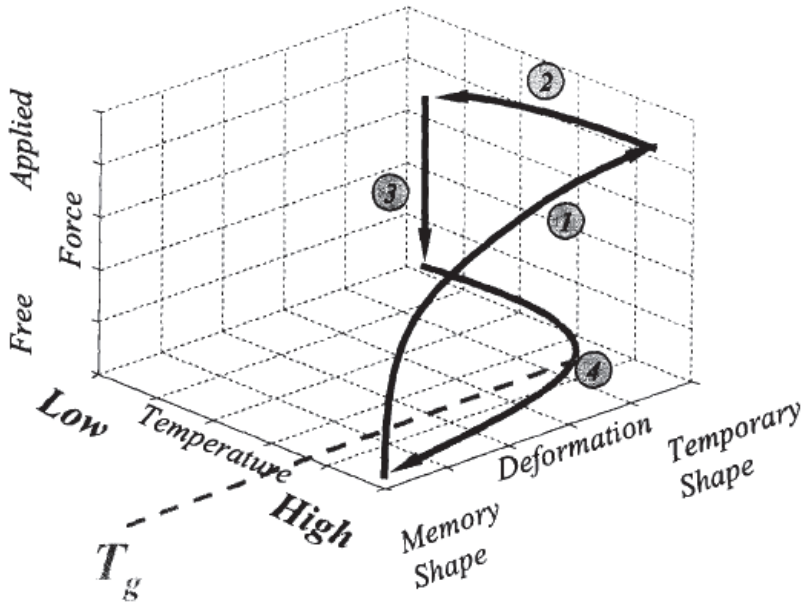

Figure 2-14. 3-D plot for SMP deformation as a function of temperature and applied force. [29]

A SMPs Young's Modulus varies greatly during its glassy and rubbery phases. Other mechanical properties(see table 2-2) do not vary nearly as significantly. The table shows property values for a polystyrene based SMP, which is the most common, SMP commercially available. It should also be noted that the SMP may have a large transition range, through which the elastic modulus will take many intermediate values.

Table 2-2. Polystyrene based SMP mechanical properties. [30]

property	SMP
T_g (°C)	62
Recovery strain, %	50-100
Actuation stress (MPa)	2-10
Young's modulus above T_g(MPa)	1240
Young's modulus below T_g(MPa)	2-10
Poisson's ratio	.3
Density (gm/cc)	.92

2.2.2 SMP Applications

SMPs also have a wide variety of uses in the aerospace sector. Many applications such as an SMP hinge, SMP composite boom and deployable optical systems can be found in [29]. One of the most interesting applications to me is that of self-healing structures. While results from most of the research in this area have been discouraging, a proof of concept by NextGen Aeronautics, The University of California and the US Army Aviation and Missile Research, Development and Engineering Center resulted in a self-healing prototype [31]. The prototype was based on mendomer, a SMP variant, with embedded magnetic particles used for activation. The mendomer was loaded with approximately 10% particle concentration, intentionally damaged and then inductively activated to induce self-healing. Figure 2-15shows the aforementioned self-healing concept, and the figure shows that after 2 minutes, the crack completely healed. No evidence of the crack was found at 100x magnification and despite the need for faster healing the proof of concept is promising.

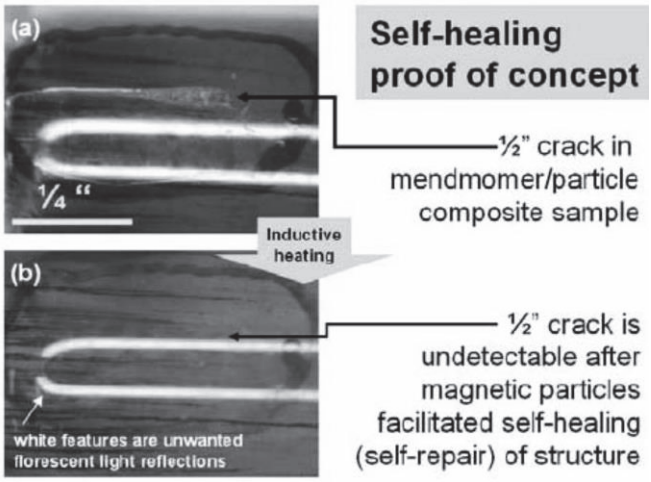

Figure 2-15. Self-healing concept. (a) sample with crack prior to healing and (b) sample after self-healing [31].

Like SMAs, SMPs also have a wide variety of applications in biomedical research. One promising area is on the improvement of current sutures. Lendlein and Langer [9]created a smart degradable medical suture to be used in minimally invasive surgical procedures, by stretching SMP fibers in their heated state (to three times their nominal length) letting them cool, then using them to loosely stitch a rat wound. The suture was then re-heated to its transition temperature, causing the thread to tighten and close the wound while applying an appropriate and controllable force of 0.1 N (see Figure 2-16).

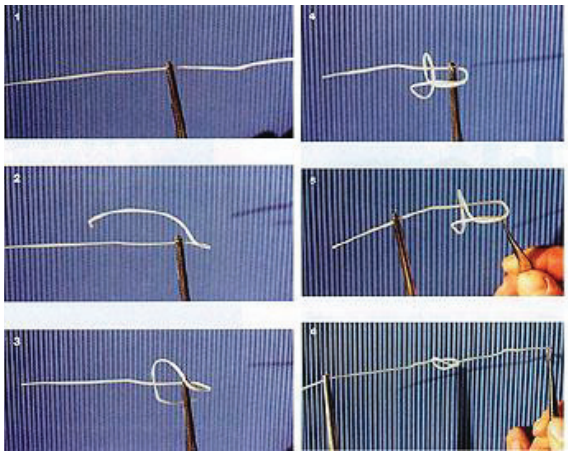

Figure 2-16. SMP suture going through stretching and re-heating process [9]

The possibility of using a shape memory polymer as a self-expandable stent (Figure 2-17) was also investigated by Wache et al in 2003 [32]. Current metal stents have several undesired side effects with blood and tissue. In an effort to solve this problem, several in vitro tests were conducted [33]. It was concluded that a shape memory polymer stent can solve many of the current complications associated with stent implanting and secondary effects incurred after surgery. The method was further investigated by implanting SMP stents in rabbits to confirm feasibility by Mei-Chin Chen,

2007 [33]. The implanted stent was found to be intact and functional without the formation of a thrombus (obstruction) after 24 hours (see Figure 2-17).

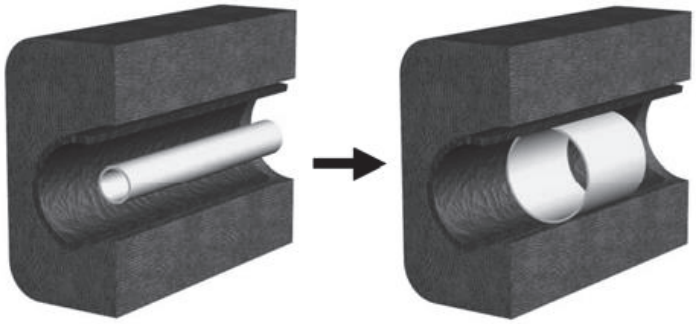

Figure 2-17. Model of SMP stent self-expanding in blood vessel. [33]

2.3 Modeling

The Literature review for the modeling of a Microvascular SMCs will begin with an overview of the modeling carried out on SMAs and SMPs individually, and then proceed to review the SMC modeling that has been conducted until now. As expected, much of the composite modeling is heavily tied to the individual component modeling.

2.3.1 SMA Modeling

Many constitutive models for SMAs have been explored [34-38]. A 3 phase model explored by Popov, [34], proposes a 3-D constitutive model based on thermodynamic potentials and on the Boyd and Lagoudas Model. Benefits of Popov's model include the ability to account for the induced stress from a phase shift from martensite to austenite and the detwinning of martensite phases. The model was

validated using a uni-axial stress state and a proposed FEM model. An additional component of the Popov's work was the exploration of mechanical wave propagation in SMA rods using the proposed model.

A Macroscopic Constitutive model was explored analytically and through finite element simulations by Thamburaja [35]. This analysis uses a micro-force balance, balance of linear and angular momentum, energy balance, the dissipation inequality and free energy densities to determine a constitutive model. Here, the proposed model was validated by a time integration procedure using ABAQUS.

Due to the large number of proposed models a comparison is required. This Comparison [36] was performed on the Tanaka Model, the Liang and Rogers Model, the Brinson Model, and the Boyd and Lagoudas Model. This work evaluates the models uni-axially for comparison. The Tanaka Model describes the stress-strain and temperature relationship solely in terms of the volume fraction (see equation 1). This equation assumes an initial phase, denoted by the 0 subscript. This model uses an exponential function to define the Martensite volume fraction, ξ. The Volume fraction is found by equation (2) for the Austenite to Martensite transformation and equation (3) is used for the Martensite to Austenite transformation.

$$\sigma - \sigma_0 = E(\xi)(\epsilon - \epsilon_0) + \theta(T - T_0) + \Omega(\xi)(\xi - \xi_0) \quad (1)$$

$$\xi = 1 - e^{(a_m)(M_s - T) + b_m \sigma} \quad (2)$$

$$\xi = e^{(a_A)(A_s - T) + b_a \sigma} \quad (3)$$

The Liang and Rogers Model uses the same constitutive form, equation (1) previously shown, but introduces a cosine function into the volume fraction model. Both

the Tanaka model and Liang Rogers model assume an initial starting phase. The volume fraction for the Liang and Rogers Model is found by equation (4) for the Austenite to Martensite transformation and equation (5) is used for the Martensite to Austenite transformation.

$$\xi = \frac{1-\xi_A}{2}\cos(\mathrm{a_m}(\mathrm{T}-\mathrm{M_f}) + \mathrm{b_m}\sigma) + \frac{1+\xi_A}{2} \tag{4}$$

$$\xi = \frac{\xi_M}{2}\cos(\mathrm{a_m}(\mathrm{T}-\mathrm{A_s}) + \mathrm{b_A}\sigma) + 1 \tag{5}$$

The Tanaka and Liang Rogers models both describe the SMA through Transformation Austenite to Martensite and vice versa, but they don't represent the twinned Martensite variant needed for OWSME and TWSME modeling, this is where the Brinson Model is used during the Martensite phase. The Brinson Model (6) accounts for this variant by introducing separate Martensite stress variables, one for stress-induced and one for temperature-induced components [37].

$$\sigma - \sigma_0 = E(\xi)\epsilon - E(\xi)\epsilon_0 + \Omega(\xi)\xi_s - \Omega(\xi_0)(\xi_{s0}) + \Theta(T - T_0) \tag{6}$$

The most general and widely used model is the Boyd and Lagoudas model which utilizes Gibbs free energy to satisfy the Second Law of Thermodynamics [38]. This model, simplified in one dimension, is very similar to the Tanaka model, but its true value is in the ability to be used in a three dimensional shape (see equation 7).

$$\sigma_{ij}^{eff} + d^1 T - \rho b_1 \xi = Y^{**} + d_{ijkl}^3 \sigma_{ij}\sigma_{kl} + d_{ij}^4 \sigma_{ij}\Delta T \tag{7}$$

The Capability of SMAs to be used as an actuator was also explored in [39]. The proposed model was constructed in MATLAB Simulink to model the proposed actuator control scheme (see Figure 2-18). In the aforementioned model the actuation control accounted for changes in temperature, electrical resistance and the hysteresis in the

phase transformations. Here, electrical heating was the method of activation. It should be noted that other activation methods could be introduced in the Simulink model in place of the electrical heating.

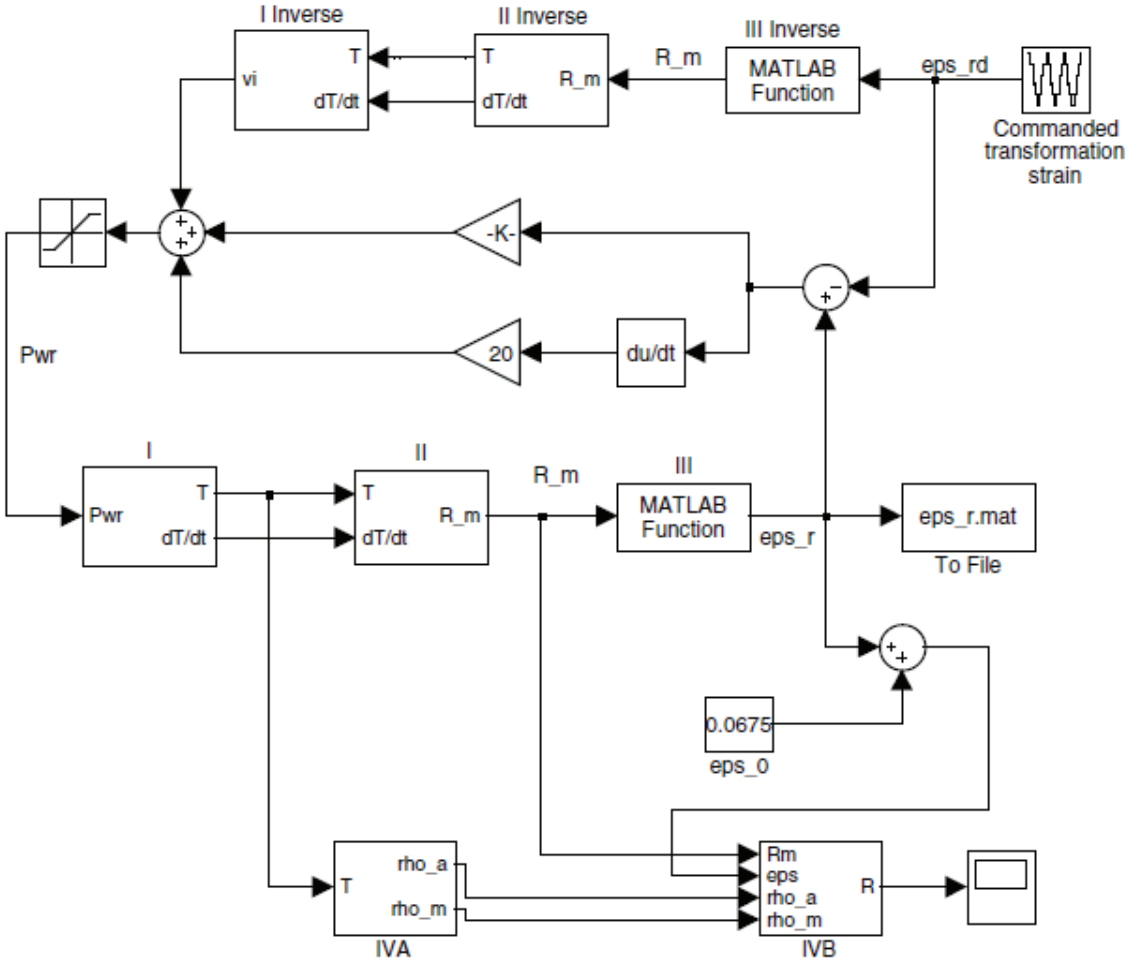

Figure 2-18. Matlab Simulink block diagram for predicting the actuation properties of SMA alloys with an electrical heating method of activation [39]

2.3.2 SMP Modeling

The SMP modeling is not nearly as extensive as the SMAs, since it is a considerably newer material class in the engineering field. However, a constitutive model has been proposed by Tobushi [40] in both linear and nonlinear forms (see equations (8) and (9), respectively). Where under large strain conditions, the non-linear model is required. This model uses a shape fixity concept to account for the locking capabilities of the SMP. Tobushi's model is the most widely used. Disscussions into further modeling on the thermal side is included in the SMC section.Constitutive models for shape memory polymers are currently limited to special cases of one-dimensional deformation.

$$\dot{\varepsilon} = \frac{\dot{\sigma}}{E} + \frac{\sigma}{\mu} - \frac{\varepsilon - \varepsilon_0}{\lambda} + \alpha\dot{T} \tag{8}$$

$$\dot{\varepsilon} = \frac{\dot{\sigma}}{E} + m\left(\frac{\sigma - \sigma_y}{k}\right)^{m-1}\frac{\dot{\sigma}}{k} + \frac{\sigma}{\mu} + \frac{1}{b}\left(\frac{\sigma}{\sigma_c} - 1\right)^{n} - \frac{\varepsilon - \varepsilon_s}{\lambda} + \alpha\dot{T} \tag{9}$$

Recent work done at the University of Pittsburgh [41] and [42] model the SMP for use in morphing aerospace skin tiles using ANSYS FEA software, analytical Ritz Raleigh energy method using the principle of virtual work (see equation 10) and strain energies (see equation 11) and experiments. Evident in these works is the need for a strong actuator and an inherent difficulty in activating an SMP thermally due to its low thermal conductivity. Thus, the need for a system with high recovery stress properties arises.

$$\delta U + \delta V = \delta \Pi \tag{10}$$

$$U = \frac{1}{2}\iiint_V \left(\sigma_x\epsilon_x + \sigma_y\epsilon_y + \sigma_z\epsilon_z + \tau_{xy}\gamma_{xy} + \tau_{yz}\gamma_{yz} + \tau_{xz}\gamma_{xz}\right)dx\,dy\,dz \tag{11}$$

2.3.3 SMC Modeling

The idea of using SMAs and SMPs in composites either together or separate components has been explored with the goal to model its adaptive performance (43-45). These works have primarily focused on a constitutive model and have done little in the way of FEA modeling.

In a recent study at OSU [43], Comsol FEA software and basic theoretical modeling were used to model three unique cases of SMC. These cases were; an axial trained SMA wire embedded at the center of an SMP, a cantilever laminate of flat SMA sandwiched in between two flat SMP layers, and an end coupled linear side by side composite. The final case was validated by experimental results.

Tobushi et al [44] also has performed modeling work on a prototype SMC laminate belt (see Figure 2-13), they considered a 3 point bend test using the basic stress case for deflection in a simply supported beam (see equation 12) and the concept of bending rigidity (see equation 13) to evaluate the bending of the composite. The 3 point bend (equation 12) can be manipulated, as Tobushi did, to solve for the activation force of the composite at the SMC's midpoint.

$$y = \frac{Wl^3}{48E_cI_c} \tag{12}$$

$$M_c = \frac{E_CI_C}{r_c} = \frac{E_{SEA}I_{SEA}}{r_{SEA}} + \frac{E_{SMA}I_{SMA}}{r_{SMA}} + \frac{E_pI_p}{r_p} \tag{13}$$

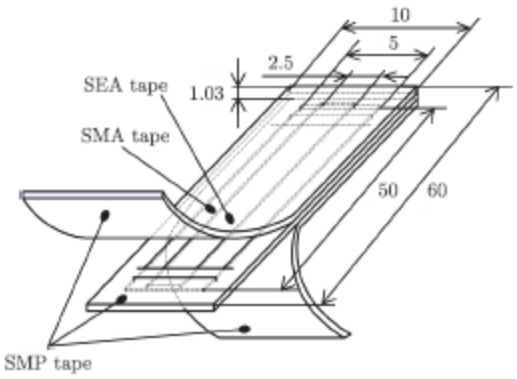

Figure 2-19. Tobushi's SMA-SMP Laminate belt Configuration. [40]

An additional model has been done by Jarali et al [45] on laminar composites using the constitutive models previously discussed in the SMA and SMP modeling sections. Specifically for the SMA, the Liang and Rogers Model (equations 1, 4 and 5) was used. Jarali also incorporated a stored strain model for the SMP (14). This model was first used by [45].

$$\frac{d\varepsilon_{St}}{dT} = \frac{E^m(\varepsilon - \varepsilon_{St} - \varepsilon_T)}{E^e}\frac{d\phi_F}{dT} \tag{14}$$

Crucial to the overall modeling of an SMC, is its thermal modeling. Thermal methods of actuation generally involve electric heating of a wire, but for the present work, the activation method will be a vascular network of tubes with a liquid delivery system as the thermal source. An investigation conducted by Phillips and Baur [46] was performed on a microvascular shape memory polymer matrix to determine a non-dimensionalized 2-D temperature distribution on the surface of the SMP. The dimensionless temperature is found by equation 15. This is used to map the solution for the temperature distribution (16) on to a known case.

$$\theta_s = \frac{T_s(y,z)-T_0}{T_s(0,0)-T_0} \tag{15}$$

$$|\theta_s| = \frac{1}{LW}\oiint_S \theta_s(y,z)\, dydz = \frac{A_0}{2}\left(\frac{2Bk}{jh_sL^2}\right)^{1/2} \sinh\left[\left(\frac{jh_sL^2}{2Bk}\right)^{1/2}\right] \tag{16}$$

3.0 Experimental Approach

The experimental approach here considered consisted of two phases. The first phase being a previous SMC work with SMA wires embedded in a SMP matrix. A brief overview of the results will be presented here. The second phase of the experimental research consisted of the characterization of the plain SMA tubes for determining their activation forces followed by their embedding process in a SMP matrix. The second phase was comprised of the investigation of two smart composites with different SMA volume percentages are presented.

3.1 Preliminary Experimentation

Flexinol SMA wires of Dynalloy, Inc., USA, (0.15mm diameter) were embedded into a commercially available SMP matrix to manufacture an adaptive composite. A photograph of the SMC can be observed in Figure 3-1. The dimensions of the SMC were 20 mm width and 60 mm length. The SMP material used was a styrene based polymer (Veriflex-S) from Cornerstone Research Group, Inc., USA.

The SMA wires were one way trained by a procedure consisting of clamping them around a metallic pipe (63.5 mm diameter) and subjecting them to a heating process in a furnace at 550°C for 30 min, followed by a quenching process in water.It was found that three heating-quenching cycles induced a new permanent curved shape in the wires. The volume fraction of wires incorporated into the SMC was between 0.5% and 1.2%. This low percentage was due to the large recovery stresses of the SMA. Indeed, the actuation forces of the SMA are up to 100 times higher than that shown by

SMPs [47].Thermal and mechanical analyses were carried out on the SMA and SMP in order to characterize their properties. Table 3-1 shows the thermal and mechanical properties.

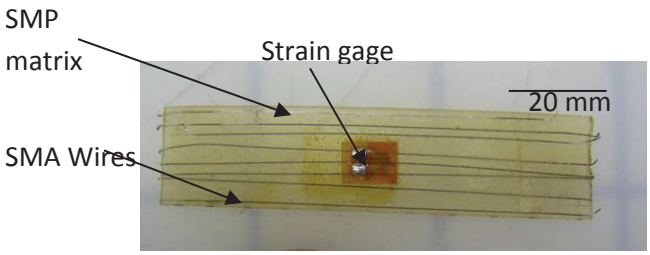

Figure 3-1. Manufactured Shape Memory Composite based on surface-embedded NiTi wires. Attached to the surface of the SMC is a strain gauge for measuring deflection.

Table 3-1. Mechanical and thermal properties of the SMA and SMP.

Material	Elastic modulus	Activation temperatures	Thermal coefficients
SMA	Austenite: 37200 GPa Martensite: 24500 MPa	Autenite (peak): 78°C Martensite (peak): 40°C	α_A=11E-6/°C α_m=6.6E-6/°C
SMP	Above Tg: 600MPa Below Tg: 0.37MPa	Tg: 65°C	α=349E-6/°C

3.2 SMA Tubes

A flat annealed SMA tube composed of Ni-Ti (from John-Mattis Inc. US.) with 1 mm ID and 0.15 mm wall thickness was used. The SMA tubes were initially one-way trained to recover a parent configuration in a curved shape. Here, the tubes were tightly clamped to a round pipe (63.5 mm diameter) and subjected to a number of heating cycles in a furnace at 550°C for 30 min followed by a quenching process in water. This training is identical to the one-way training performed on the SMA wires previously studied (see section 3.1).In order to induce a Two-Way Shape Memory Effect (TWSME) on the SMA tubes, an additional procedure was followed. The tubes were exposed to a number of thermo-mechanical cycles where they were stretched up to 1% of their nominal strain followed by a heating process above their austenite temperature. To ensure the tubes were thermo-mechanical stable after the two-way training, they were subjected to more than 100 heating-cooling cycles and their TWSME was confirmed. Figure 3-2 shows the TWSME on the SMA after heating the sample up to 120°C for two minutes followed by a cooling process to room temperature.

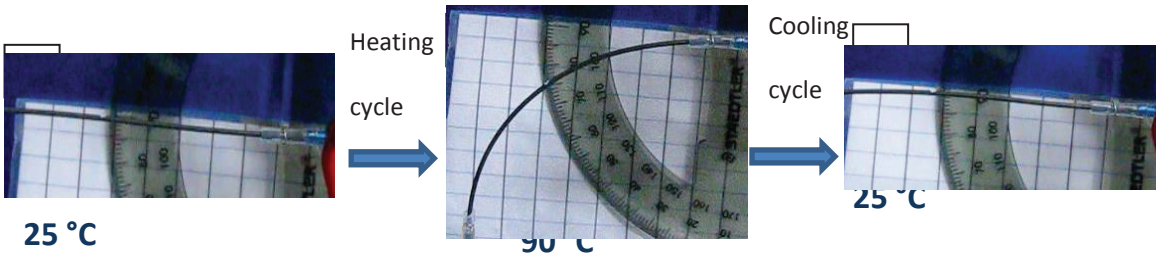

Figure 3-2. TWSME on the SMA tube following a heating-cooling cycle using ethylene glycol as the thermal activation fluid. a) initial state b)fully active c) return to initial state after cooling. [48]

A Differential Scanning Calorimeter (DSC) analysis in a TA Instruments Q100 was performed on the SMA tubes to measure the austenite and martensite temperatures of the TWSME tubes. Knowing these temperatures is imperative for the selection of the appropriate transition temperature for the SMP used. Additional testing was performed on the SMA tubes on an Universal Instron Machine with a temperature controlled environmental unit to determine their activation forces as a function of temperature. The final component of testing for the SMA tubes was conducted in a pump set-up to verify the SMA's TWSME and to determine the angle of deflection based on the temperature of the SMA.

3.3 Microvascular SMC

A styrene based SMP (Veriflex-S) from Cornerstone Research Group, Inc., USA was used as the SMP matrix in the composite. Here, steel rods of 1.3 mm diameter coated with a release agent were embedded into the mid-plane of the SMP material. The polymeric matrix within the steel rods was cured flat in an enclosed cast mold following the instructions of the material's manufacturer. Following the curing process, the panel was removed from the mold and the steel rods were carefully removed from the matrix. The removal of the rods left cylindrical channels in the SMP that were subsequently filled by the two-way trained SMA tubes. In order to enhance the adhesion between the microvascular SMAs and the SMP, a fast curing epoxy was applied at their common interface. The panel was cut in coupons of 20 mm width and

60 mm length. Figure 3-3 shows the completed microvascular SMC assembly. Here, the manufactured SMC was based on 1.3% or 2% volume fraction of SMA (2 or 3 tubes, respectively). This volume fraction was chosen based on the initial research work established in section 3.1. Indeed, a 1.3% or 2% volume fraction of the SMA tubes in the SMC would ensure that the microvascular SMC will exhibit an adaptive performance based on the TWSME of the alloy. A DSC analysis was also carried out on the SMP to characterize its T_g and to ensure that when the SMA is activated the SMP is in its rubbery phase in order to be fully controlled by the microvascular phase.

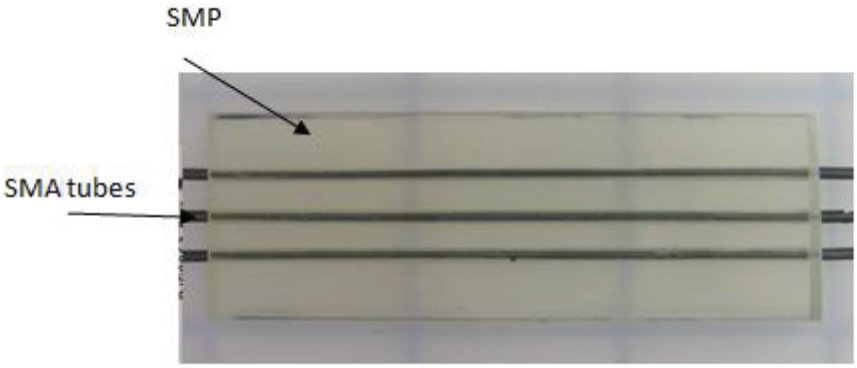

Figure 3-3. Micrograph of the manufactured microvascular SMC with a VfSMA = 2%.

The final component of testing for the vascular SMC was conducted using the aforementioned pump set-up for the single SMA tube (see figure 3-4). The activation fluid used was mono-ethylene-glycol (MEG), and the pump system was used to provide measurable and consistent flow rates for the heating and cooling process. Due to safety and reservoir restrictions, the flow rate during the heating cycle was conducted at 15 mL/min while the flow rate during the cooling process was conducted at 25 mL/min. An

additional reason for the difference in flow rates was to ensure that the SMA completes its cooling cycle before the SMP begins to cross its glass transition temperature back to its glassy phase. During the adaptive testing an infrared camera was used to record the thermal profile of the SMC, whereas a digital camera was used to record its out of plane deflection.

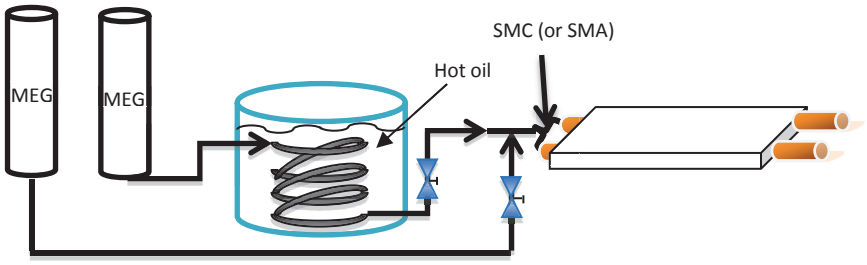

Figure 3-4. Schematic of the heating-cooling pump system. The system shows a hot bath oil for heating the MEG during the activation process. [48]

4.0 Theoretical Modeling

A thermal transient analysis has been performed on the SMC, and the numerical results have been used in the mechanical theory to compare with the experimental and FEA Results in the deflection of the SMC. For this work, the SMA's temperature has been assumed to be perfectly uniform due to its thickness and its relatively large thermal conductivity and therefore, non-existent transient behavior has been considered. It has also been assumed that the thermal profile of the SMC is governed by the thermal behavior of the SMP during the microvascular activation process with respect to time, despite the fact that the SMA provides the activation forces under the thermal stimulus supplied by the vascular fluid network.

4.1 Thermal Analysis

The goal of the thermal analysis was to find the temperature distribution through the composite with respect to its transient behavior. The standard 3-D transient heat equation for an isotropic material is shown in equation 17.

$$\frac{dV}{\alpha}\frac{d\,T}{dt} = \frac{d^2T}{dx^2} + \frac{d^2T}{dy^2} + \frac{d^2T}{dz^2} \tag{17}$$

The following assumptions and Boundary Conditions were then applied to the heat equation for this analysis. 1) The microvascular fluid was not analyzed, since it was assumed to have a constant and uniform temperature profile during the heating and cooling processes. This leads to the assumption that the SMA is at a uniform temperature, and is equal to the thermal delivery fluid.2) An infinite wall assumption

which ignored end effects producing a 2-D transient thermal model. 3) The coupling of the inner SMP and outer SMA walls, which applies the temperature of the SMA and assumes an interchangeable heat flux between boundaries. These assumptions, in addition to the natural convection on all outer walls and symmetry, lead to the following mathematical model and boundary conditions (see equations 18-21).

$$\frac{dA}{\alpha}\frac{d\,T}{dt} = \frac{d^2T}{dy^2} + \frac{d^2T}{dz^2} \tag{18}$$

Symmetry conditions were also applied to the whole SMC to produce a quarter of the geometry in the analysis. The thermal symmetry was considered, since the symmetry boundary has no heat flux normal to the boundary. Therefore, at y=0 and atz=0, the following boundary condition is applied (see equation 19).

$$\frac{dT}{d(x\ or\ y)}=0 \tag{19}$$

Convection boundary conditions were also applied to the surfaces exposed to the ambient environment, in this case, the side and top sections. Here, the direction of heat flux normal to the surface was given by equation20.

$$\frac{dT}{d(x\ or\ y)} = hA(T - T_\infty) \tag{20}$$

The outer wall of the SMA and the inner wall of the SMP were also considered to be coupled. The coupled boundary assumed that there is no temperature difference between the two walls and that the heat flux is constant through the boundary. Since it was determined that the temperature drop across the SMA's thickness was negligible, the fluid temperature was assumed to be that of the entire SMA. Hence:

$$T_{SMA,\,r_o} = T_{SMP,r_o} = T_{fluid} \tag{21}$$

Indeed, transient analysis requires an Initial Condition, and room temperature was chosen for this analysis. For the cooling cycle, the initial condition was considered to be the temperature distribution at the end of the heating cycle.

$$T_i = 22℃ = 295K \quad (22)$$

Irregular geometric boundaries on the SMP made the use of a direct solution through a differential model a difficult task. Five physical boundaries are present and only four permitted boundary conditions in a 2-D differential model. Numerical methods were therefore used to attain an approximation to the solution of the differential model. Here, the Eulerian Explicit time marching was chosen (see equation 23). This method has a distinct advantage over other transient numerical methods, since it uses all known values with respect to the current time-step to determine the future time-step's value. This advantage, allows for the solution to be attained without solving simultaneous equations. The main drawback of this method is that it requires a stability criterion to ensure the solution converges. These conditions are graphical represented in Figure 4-1. along with the numerical mesh.

$$\frac{\Delta x \Delta y}{\alpha}\frac{T_{i,j}^{n+1}-T_{i,j}^{n}}{\Delta t} = \sum_x \frac{\Delta y}{\Delta x}\left(T_{i\pm\Delta x}^{n} - T_i^n\right) + \sum_y \frac{\Delta x}{\Delta y}\left(T_{j\pm\Delta y}^{n} - T_j^n\right) + \sum_{convection} \frac{hA_h}{k}\left(T_\infty - T_{i,j}^n\right) \quad (23)$$

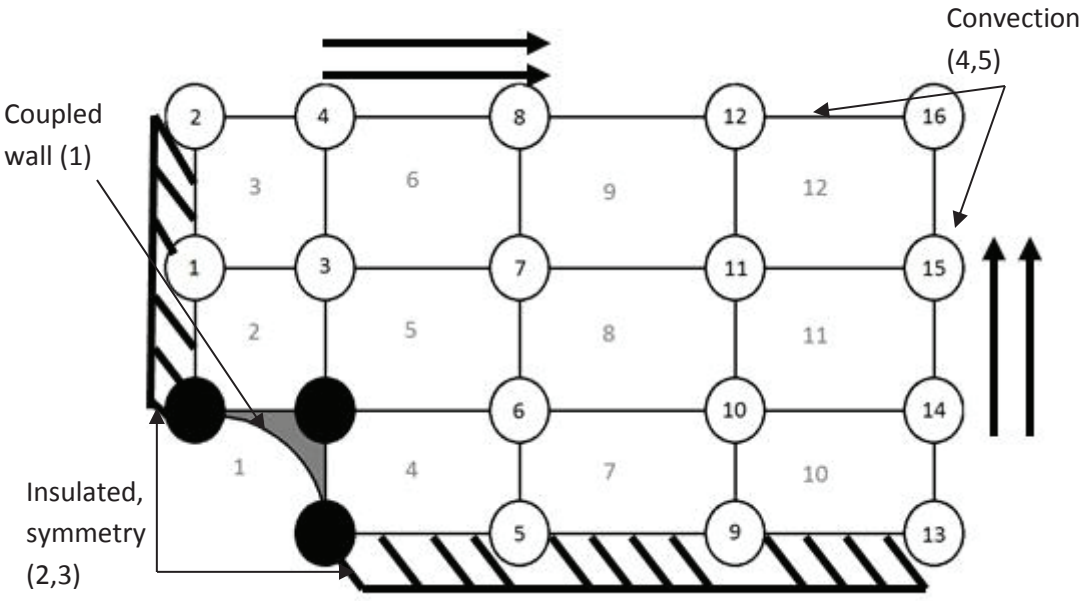

Figure 4-1. Numerical mesh and Boundary Conditions.

The numerical solution can be simplified using matrices to the form of equation 24. This solution applies to all geometric cases. The values in each component of the equation change for each geometric case. The T and X vectors are the nodal temperature values for the next and current time steps, respectively. A is the matrix of coefficients of the current time-step nodal temperatures, and B, is the vector composed of the known temperatures created by the boundary conditions. The B vector can be combined or separated from the A and X matrices for convenience.

$$T = AX + B \tag{24}$$

Where, $T = [T_1^{m+1}, T_2^{m+1}, \ldots, T_n^{m+1}]$ where m denotes the time-step

$X = [T_1^{m}, T_2^{m}, \ldots, T_n^{m}]$

4.2 Mechanical Modeling

The numerical results were used to determine the Elastic modulus for each numerical element of the SMP. A Composite beam Analysis was then performed using the numerical thermal results to evaluate equivalent an EI for the composite (see equation 24), this was subsequently used for determining the deflection of the composite (equation 25). The second moment of inertia, I, was determined for each element and E was determine by using the temperature found in the numerical analysis against the known elastic modulus.

$$(EI)_{SMC} = \sum_{i,j} E_{i,j} I_{i,j} \tag{25}$$

Analytical modeling was initially studied using a basic static composite beam analysis on the SMC using classical bending theory (see equation 25). While these equations do not account for the training or internal activation of the material, they are valuable due to the fact that they determine whether the SMC will be able to fully actuate to pre-trained deflection, based on the mechanical properties of the material. A parametric study using this modeling approach was used to optimize the SMA by volume in the SMC.

$$\delta(x) = \frac{Fx^2(3L-x)}{6(EI)_{SMC}} \tag{25}$$

The deflection was found at the end of the SMP section. This location is also where the deflection was recorded experimentally for comparison purposes. The load was assumed to be applied at the end of the SMA tube (see figure 4-2 for the load case).

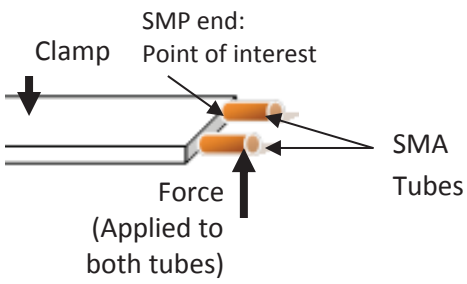

Figure 4-2. Mechanical SMC loading case.

5.0 Finite Element Modeling

The Microvascular SMC was studied using several Finite Element Models, created in the ANSYS FEA Software (Version 13.0). The modeling was initially performed on the SMA tube by itself to model its actuation without the presence of the SMP, under thermal and mechanical cases. The analysis was then incorporated into the SMP to analyze the composite as a single structure. The transient thermal analysis was run using Fluent FEA software. The thermal results were imported into the mechanical solver as a temperature load on the SMP. The exposed SMA section (SMA not covered by SMP) was included to match the experimental setup. For each experimental geometric case, an FEA model was performed. Additional models were then used to validate be used to predict the optimal design for the SMC based on SMP thickness.

5.1 Model Geometry and Symmetry

The possible symmetries used for the thermal modeling for the SMA are axisymmetric, quarter and half. Mechanically, only half symmetry was considered due to the nature of the loading. Therefore, half symmetry was used for the coupled thermo-mechanical modeling. In the thermal modeling, the working fluid zone for the ethylene glycol had the same symmetry limitations as the SMA, but was suppressed for the mechanical side of the modeling. The model symmetry was based on the overall geometry per unit SMA tube in the SMC. The experimental setup included either two or three SMA tubes, with OD, ID and length equal to, 1.3 mm, 1.0 mm and 100 mm, respectively. These tubes were embedded at the center of the SMP, with height, width

and length equal to 3.404 mm, 20 mm and 60 mm, respectively. When the width of the analyzed geometry was determined, it was assumed that the SMA tubes were equally spaced in the SMC. This resulted in a width of 6.67 mm and 5 mm for the two and three tube cases, respectively (see Figure 5-1).

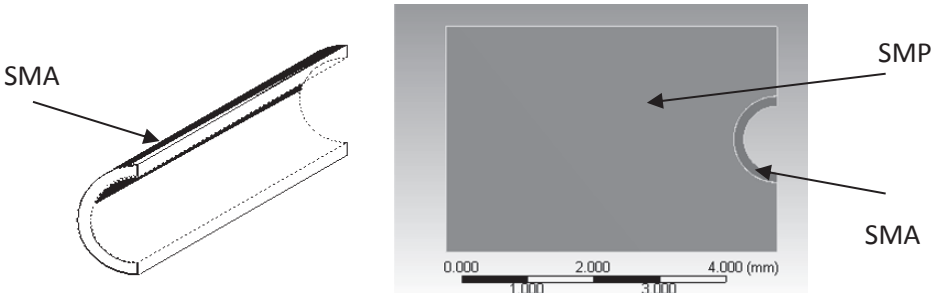

Figure 5-1. Model symmetries (left) SMA (Right) SMC.

5.2 Mesh

The Final mesh used for the SMC is shown (with fluid suppressed) in Figure 5-2. When analyzing components of the SMC individually, such as the SMA and SMP, the same mesh was used on the individual section for continuity. The model was validated against experimental and analytical results. Due to the irregular boundary nature of the SMP and the symmetry used, the mesh has a few non-ideal elements. Here, an inflation mesh condition was applied on the y-z planar faces of the fluid and SMP sections, to transition from the curved shared boundaries of the SMA to the square boundaries of the SMP. The mesh applied was identical for all the SMC cases studied, and no mesh constraints were applied to top and bottom edges of the SMP geometry. This allows the software to make whatever size and number elements across them to satisfy the rest of the constraints applied.

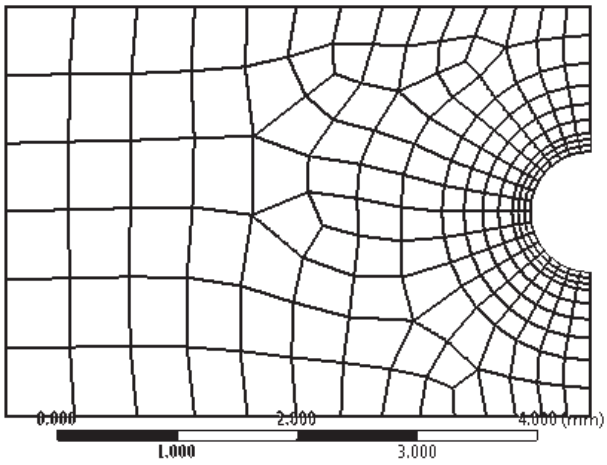

Figure 5-2. SMC Mesh.

5.3 Fluid-Thermal Modeling

The Fluid-Thermal modeling consists of two parts. The first was the thermal transient analysis of the SMA alone. And the second was performed on the SMC. This was performed for the purpose of determining the behavior of SMA as well as for the completion of the analysis of the SMA through a full thermo-mechanical cycle. For modeling consistency, the fluid flow was always oriented in the positive x-direction within the ANSYS geometry. The SMA was not expected to have a very long transient period or have a very large temperature distribution, due to its thickness and quick experimental activation.

The working fluid considered was ethylene glycol, as in the experiment. The fluid velocity profile was not of particular concern in this resarch work since its flow rate is fairly low and the fluid wasjust used as a thermal delivery medium rather than a contributor to the mechanical activation or stabilizer of the SMA. Indeed, at larger scales

the fluid may become a concern for design. The material properties of the ethylene glycol are shown in Table 5.1. The fluid model used was turbulent k-epsilon model, this is primarily due to the presence of the thermocouple at the entrance of the SMA tube.

The Boundary conditions used are as follows. 1) The fluid inlet was given a prescribed temperature of 373 K (100°C) and a mass flow rate of 0.000278 kg/s (15 mL/min) for heating and295 K (22°C) with a flow rate 0.000463 kg/s (25 mL/min) for cooling. The reason for the difference was to match the experimental setup. 2) Symmetry boundary conditions were applied to the centerline plane(xy) of the SMA, on all parts of the SMC. 3) Coupled wall interfaces were set up between the glycol fluid zone and the inner wall of the SMA. Coupled surfaces impose the same temperature and flux in each coupled wall boundary condition. All exposed surfaces surfaces were given a convection boundary with the ambient air at 295 K and a convection coefficient, h, equal to 8 W/ m^2K (determination of the h value is discussed in the next section).

Table 5-1. Ethylene Glycol Fluid Properties.

Density (kg/m^3)	1111.4
C_p, specific heat (J/kg-K)	2415
k, Thermal Conductivity (W/m-K)	0.252
μ, viscosity (kg/m-s)	0.0157

5.3.1 Determination of the Convection Coefficient, h, for ambiant environment.

The convection coefficient h was determined by comparing the theoretical steady state temperature drop with that of the experimental steady state set-up.Here, the h value was determined between the maximum and minimum values for natural convection in air(5 and25 W/m^2K, repectively) [52]. Using the experimental steady state

temperature and the basic convection equation, the h value of 8 W/m^2K was agreed upon.

5.4 SMA Modeling

The modeling was initially performed on the SMA tube by itself to model its actuation without the presence of the SMP, under thermal and mechanical cases. The following is an outline of the procedure performed to accomplish this, both thermally and mechanically.

5.4.1 SMA Fluid-Thermal Analysis

The SMA and glycol Fluent model boundary conditions are shown in Figure 5-3. The fluid thermal model was performed using axisymmetric, quarter and half symmetries to show result convergence. The outer fluid wall and the inner SMA wall were coupled thermally. This means that the temperature was equal at the SMA-glycol boundary. This is a common heat transfer assumption because the thermal and fluid boundary layers are included within the turbulent fluid model applied to the ethylene glycol fluid.

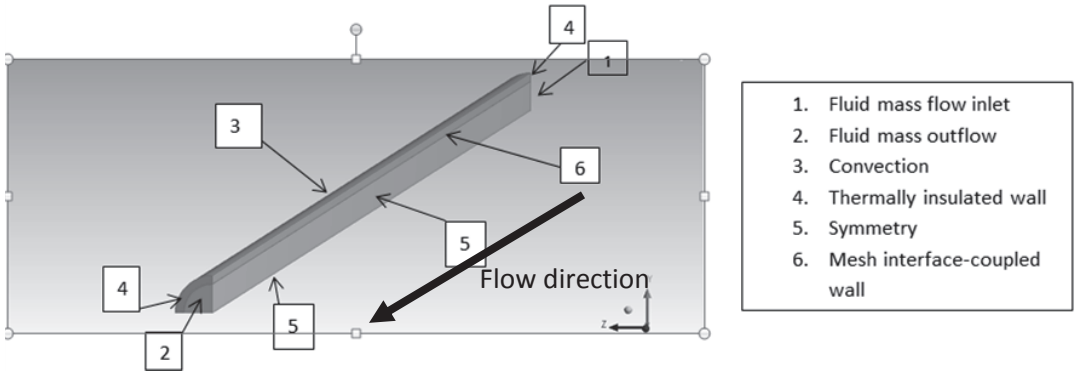

Figure 5-3. Boundary conditions for the SMA-fluid (shown for a quarter symmetry).

5.4.2 SMA Tube

The mechanical actuation of the plain SMA tube was modeled considering a local point load at the end of the SMA. The mechanical boundary conditions applied to the SMA are shown in Figure 5-5.During the Mechanical modeling the fluid was suppressed, based on the assumption that the fluid driving pressure does not significantly affect the actuation of the SMA. The displacement condition applied to the symmetry plane allows no deflection normal to it (δ_z=0). To complete the symmetry condition rotation, through the plane was also restricted. This was accomplished by applying the displacement restriction to both the top and bottom faces of the symmetry cut (preventing rotation about the x-axis) as well as to the entire length of the cut faces, preventing rotation about the y axis. This modeling was performed to validate the behavior of the SMA tubes within the FEA simulation against the experimentally recorded behavior.

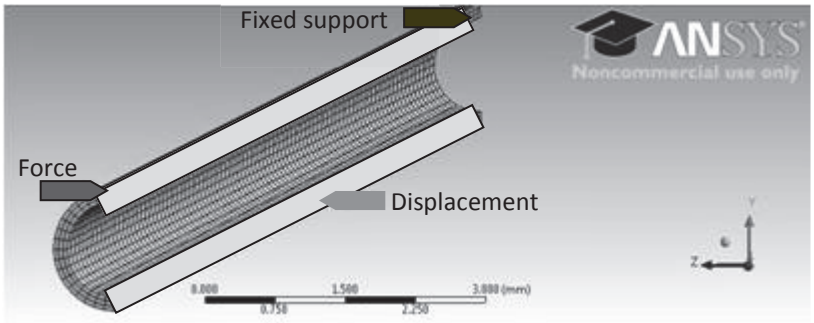

Figure 5-4. Mechanical Boundary Conditions on SMA.

5.5 SMC Coupled Thermo-Mechanical Modeling

The coupled thermo-mechanical model used the temperature distribution found in fluid-thermal analysis and used ANSYS Workbench to import the temperature distribution into the setup of the static structural analysis. The primary modeling to duplicate the experimental results was done in two cases. The first case used the point load at the end of the SMA. This load data was experimentally recorded on the temperature controlled Instron machine. These results are based on a cantilever approximation of the SMA, and consequently, only the end deflection of the SMA can be validated by this case. Once the SMA's end deflection was verified, the second case used the complete SMC geometries, again with the point load at the end of the SMA and the imported temperature load from the fluid-thermal analysis. The coupled analysis setup for workbench is shown in Figure 5-4.

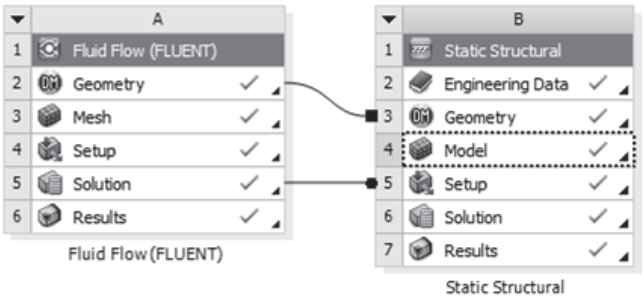

Figure 5-5. Workbench project chart.

Tables 5-2 and 5-3 show the material property data for the SMA and SMP that was used in the FEA. The mechanical analysis used the Young's Modulus (E), Poisson's ratio (ν) and the Coefficient of Thermal Expansion (α) (see Table 5-2). The thermal analysis required the input of the density (ρ), thermal conductivity (k) and specific heat (c_p) of the solid materials (see table 5-3). Additional properties are internally computed by the software such as the thermal diffusivity, α_T. It should be noted that the mechanical properties of the SMA and SMP vary greatly with temperature while the thermal properties are isotropic and nearly constant as they are based primarily on the chemical composition of the material.

Table 5-2. Mechanical Properties.

	SMA			SMP		
T (°C)	E (MPa)	ν	α	E (MPa)	ν	α
20.35	24500	0.3	6.60E-06	827.423	0.48	8.97E-09
26.96	24500	0.3	6.60E-06	751.344	0.48	8.97E-09
32.61	24500	0.3	6.60E-06	676.137	0.48	6.91E-08
37.92	24500	0.3	6.60E-06	593.168	0.48	1.20E-07
42.56	24500	0.3	6.60E-06	510.232	0.48	1.47E-07
47.47	24500	0.3	6.60E-06	408.863	0.48	1.85E-07
54.73	24500	0.3	6.60E-06	234.857	0.48	2.47E-07
59.80	24500	0.3	6.60E-06	123.574	0.48	2.94E-07
65.55	24500	0.3	6.60E-06	49.602	0.48	3.63E-07
70.63	24500	0.3	6.60E-06	21.472	0.48	3.97E-07
75.67	24500	0.3	7.70E-06	8.034	0.48	5.25E-07
80.04	27500	0.3	8.80E-06	2.612	0.48	6.99E-07
86.83	33200	0.3	9.90E-06	0.816	0.48	7.63E-07
91.58	34500	0.3	1.10E-05	0.527	0.48	7.91E-07
97.74	36500	0.3	1.10E-05	0.384	0.48	8.03E-07
102.24	36500	0.3	1.10E-05	0.335	0.48	8.03E-07
104.13	36500	0.3	1.10E-05	0.323	0.48	8.03E-07
106.99	36500	0.3	1.10E-05	0.311	0.48	8.03E-07

Table 5-3. Thermal Properties.

	SMA	SMP
ρ (kg/m^3)	6450	920
k (W/(m*°C))	18	0.17
c_p J/(kg*°C)	836	1800

5.5.1 SMC Transient Thermal Analysis

The combination of the SMA and SMP in the SMC modeling requires the addition of a coupled boundary condition between the the outer wall of the SMA and the inner wall of the SMP. Hence, the remaining procedure was the same as the analysis of the SMA tube alone. The analysis was performed out for the two and three tube

experimental geometries (1.3% and 2% SMA by volume), with the tubes assumed to be evenly spaced.

5.5.2 Coupled SMC

The Thermo-Mechanical modeling of the SMC follows a nearly identical procedure to that performed on the SMA. In addition to the Boundary conditions on the SMA, the end of the SMP is fixed as well as the exposed end of the SMA that is between the ends of the SMA and SMP were fixed(see Figure 5-6). This is because the experimental SMC was constrained in a like manner and didn't allow the SMA to bend outside the fixed end of the SMP. Additionally, symmetry conditions were also applied to the faces on the symmetry plane on the SMP to provide model stability (δ_z=0). This procedure was repeated for each of the cases analyzed. Here, the default bonded contact assignment between the SMA and SMP on its interface was used.

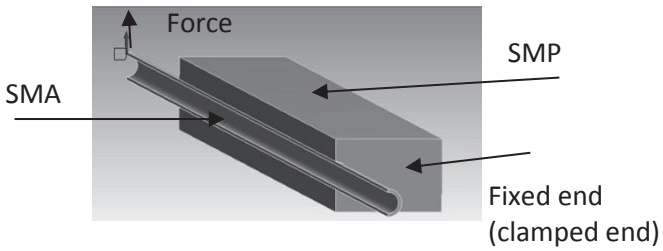

Figure 5-6. SMC Mechanical Boundary Conditions

6.0 Results and Discussion

This chapter will present the results found in this work, starting with the experimental findings, followed by the theoretical and FEA outcomes. For comparison purposes the experimental results will be considered the most accurate. Each section will present the results for both the SMA individually and the SMC. The results presented in this section will focus on, the minimum temperature found in the SMC, the time to reach steady state for the SMC, the minimum temperature at steady state and the deflection at the end of the SMP within the composite. A discussion of the results geared toward optimization and future work will also be presented.

6.1 Experimental Results

The experimental results presented for the SMA alone will include the angle and deflection achieved based on the temperature and the force as a function of temperature. The SMC experimental results will focus on the deflection at the end of the SMP and the temperatures observed by a thermal camera on the SMC's surface.

6.1.1 Experimental Results: SMA

The angle of deflection achieved by the SMA was determined by recording the angle from the original SMA configuration at the free end to the morphed shape at the free end(see figure 6-1). This was done so that the experimentally recorded forces could be broken into components for their use in the FEA. The compiled results for angle temperature and force recorded experimentally are shown in table 6-1 and figure 6-2.

The deflection at the end of the SMA alone was found to be approximately 60 mm. The FEA simulation on the single SMA tube was performed to duplicate this result.

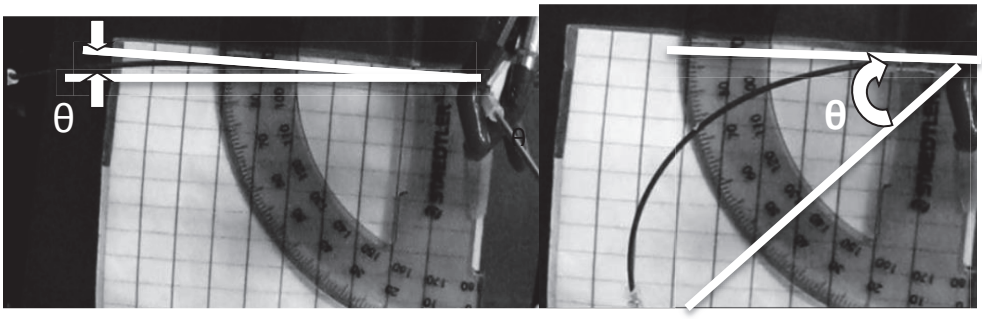

Figure 6-1. Out of plane deflection angle of the SMA tube through the heating-cooling cycle. (left) initial starting angle, θ=0° in data (right) max angle achieved, θ=45°

Table 6-1. Out of plane deflection angle and force data as a function of temperature.

Temperature [C]	Angle of Deflection [Degrees]	Force [N]
26.2	0	0
42.8	10	2.1
60.5	30	6.3
69.9	35	11.5
77.2	39	17.8
100.2	43	42
105	45	47
95.7	42	39
77.8	40	42
54.7	35	27
49	30	16
45.4	24	9.9
43.1	16	6.1
41.5	10	3.2
39.7	5	0.5
34.9	0	0

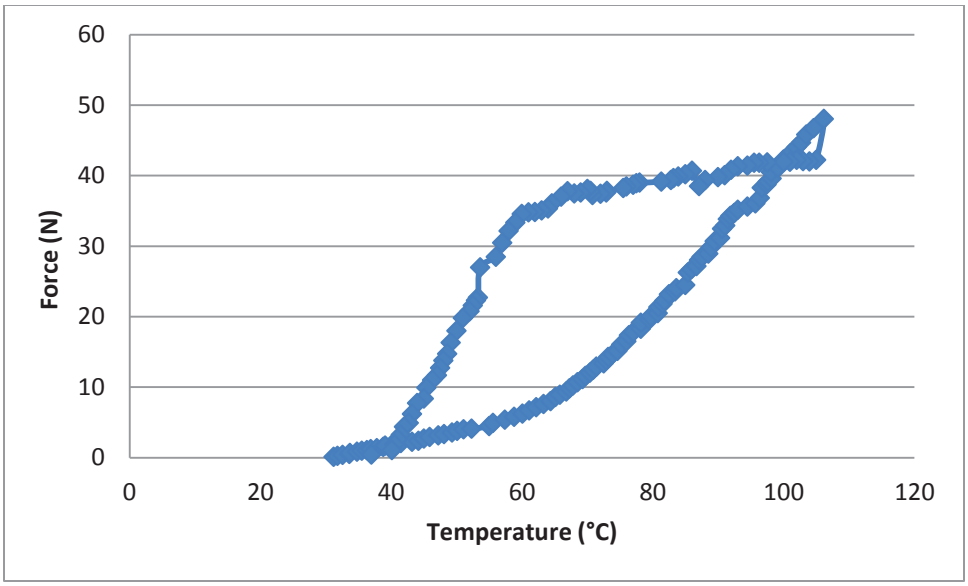

Figure 6-2. Recorded actuation force as a function of temperature.

6.1.2 Experimental results: SMC

The results recorded from the experimentation on the SMC focused on the final deflection at the end of the thermal heating cycle (max deflection) and the temperature on the surface of the SMP (and exposed SMA sections) as recorded by a thermal camera. The deflection is shown in figure 6-3. The two tube case (1.3% $V_{f,SMA}$) had almost 10 mm of observed deflection and the three tube case (2%$V_{f,SMA}$) had approximately 13 mm of deflection. There is some reader error in the approximation of this measurement. It can also be seen in the figure that the SMC returned to its starting point at the end of the cycle, indicating this process is completely reversible.

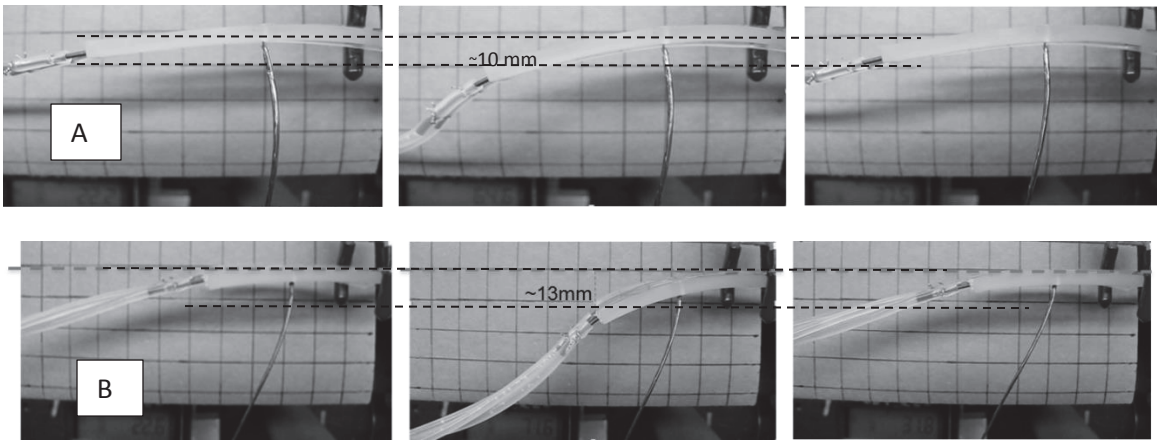

Figure 6-3. Observed deflection on the SMC through cycle (left) start of cycle (middle) max deflection, (right) end of cycle a) 2 tubes, max deflection ~ 10 mm. b) 3 tubes, max deflection ~13 mm.

The thermal data recorded focused on the minimum temperature observed on the SMC surface (see Figure 6-3) which is the side section of the SMC as recorded by the thermal camera. Due to the semi-transparent nature of the SMP the side view may have some error of the warmer temperatures showing through the SMP. It can be seen that the SMP is almost uniform temperature across the composite at the end of the heating process.

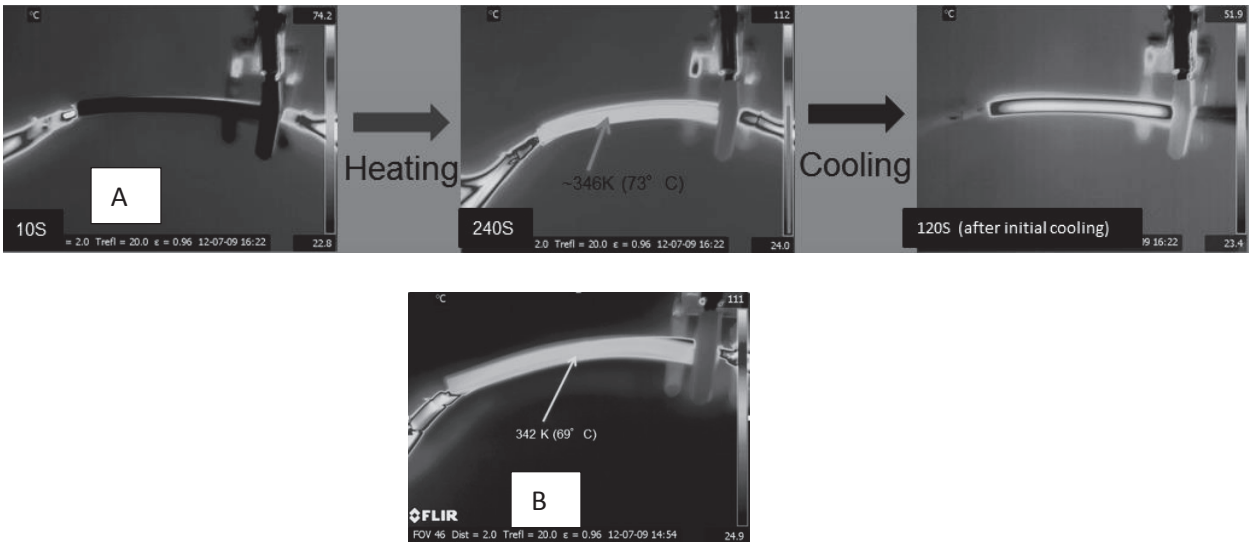

Figure 6-4. Thermal results of the vascular SMC following a heating-cooling cycle a) SMC based on 3 tubes yielding a temperature of 73°C on the edge of the surface at the maximum out of plane deflection b) SMC based on2 tubes yielding a temperature of 69°C on the edge of the surface at the maximum out of plane deflection.

The top side of the SMC was also recorded during the heating-cooling cycle (see Figure 6-4). This was performed to determine if there was error present in the images taken from the side due to the transparency of the SMP. The temperature observed from the top view confirms that the SMP's partial transparency does affect the read temperatures as the new edge temperatures on the SMP are 59°C and 67°C, for the 1.3% (two tubes) and 2% (three tubes), respectively. This is a significant drop in temperature. The top view also presents an additional behavioral observation during the cooling cycle. It was observed that the SMP stored some of the heat in the regions far from the SMA highlighting the low thermal diffusivity of the SMP. Indeed, the hot section in the SMP could potentially reactivate the SMA tubes. It is also expected that the time to return the SMC to Room temperature is nearly half that of heating because

of the difference in the volumetric flow rates of the fluid for the experiment, recall: 15 mL/min for heating and 25 mL/min for cooling.

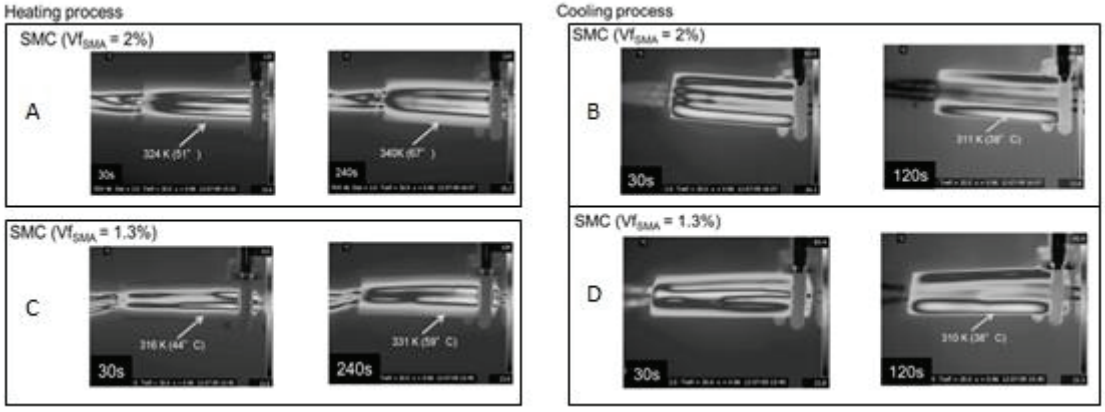

Figure 6-5 . Top view of SMC thermal results. (A) & (B) represent heating and cooling for the 2% $V_{f,SMA}$ (3 tubes) (C) & (D) represent heating and cooling for the 1.3% $V_{f,SMA}$ (2 tubes)

Note: the time indicated on the cooling side is after the cold fluid is started through the microvascular delivery network.

6.2 Theoretical Results

The theoretical results focused primarily on the thermal analysis of the SMC. This thermal analysis was subsequently used in the mechanical analysis of the SMC. Some preliminary results on the SMA were also performed and will be presented first.

6.2.1 Theoretical Results of Plain SMA Tubes

The assumption that the temperature difference across the thickness of the SMA is negligible was validated using the conduction equation. It was found that the temperature drop across the thickness of the SMA was 0.0052°C, at Steady state. This

assumption is also validated by the observation during the experiments that the SMA surface visible appears to be at the temperature of the fluid.

6.2.2 Theoretical results: SMC

The first analysis of the SMC using basic beam analysis assumed a constant temperature across the whole composite. Here the Beam analysis was based on a SMA-SMP counterbalance forces and it was observed that at $V_{f,SMA}$ greater than 1% the SMC is fully controlled by the alloys (see Figure 6-6). This result was from the preliminary research on the SMA wires [49].

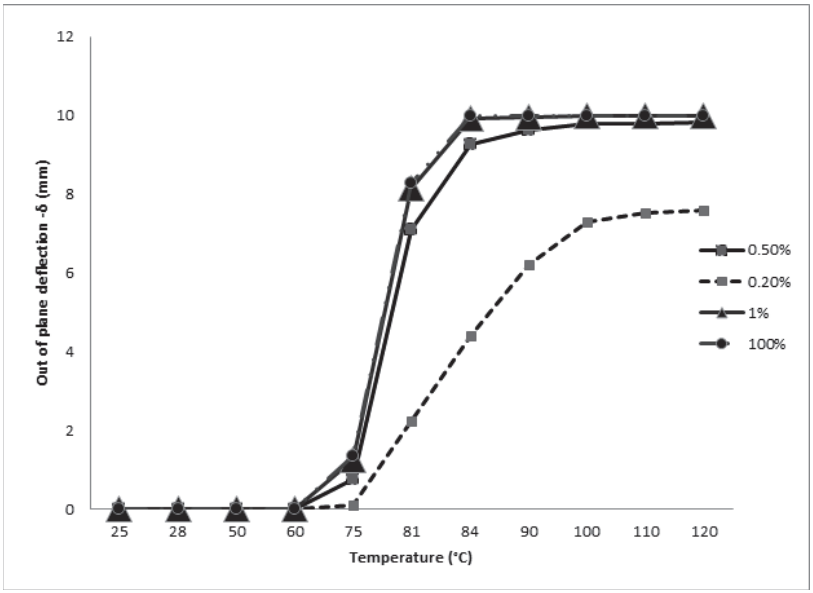

Figure 6-6. Effects of the percent volume of the SMA in SMC on its deflection. [49]

The thermal transient analysis of the SMC through its heating cycle gives an indication of the tube spacing required to achieve the actuation against time. The transient thermal analysis is shown in Figure 6-6. Here, a convergence criterion of

$10x10^{-4}$was used in the numerical analysis. The minimum temperature in the SMC is directly related to the time required for the SMP to be fully activated. The transition temperature of the SMP is 65°C. From the figure, it can be observed that for less than 3 tubes ($V_{f,SMA}$ =2%) it would take over 100s for the SMP to pass its glass transition temperature at every point in the composite. Indeed, a SMC based on a single SMA tube ($V_{f,SMA}$ =0.65%),the SMP never reaches its T_g, therefore never achieving a fully activated SMC.

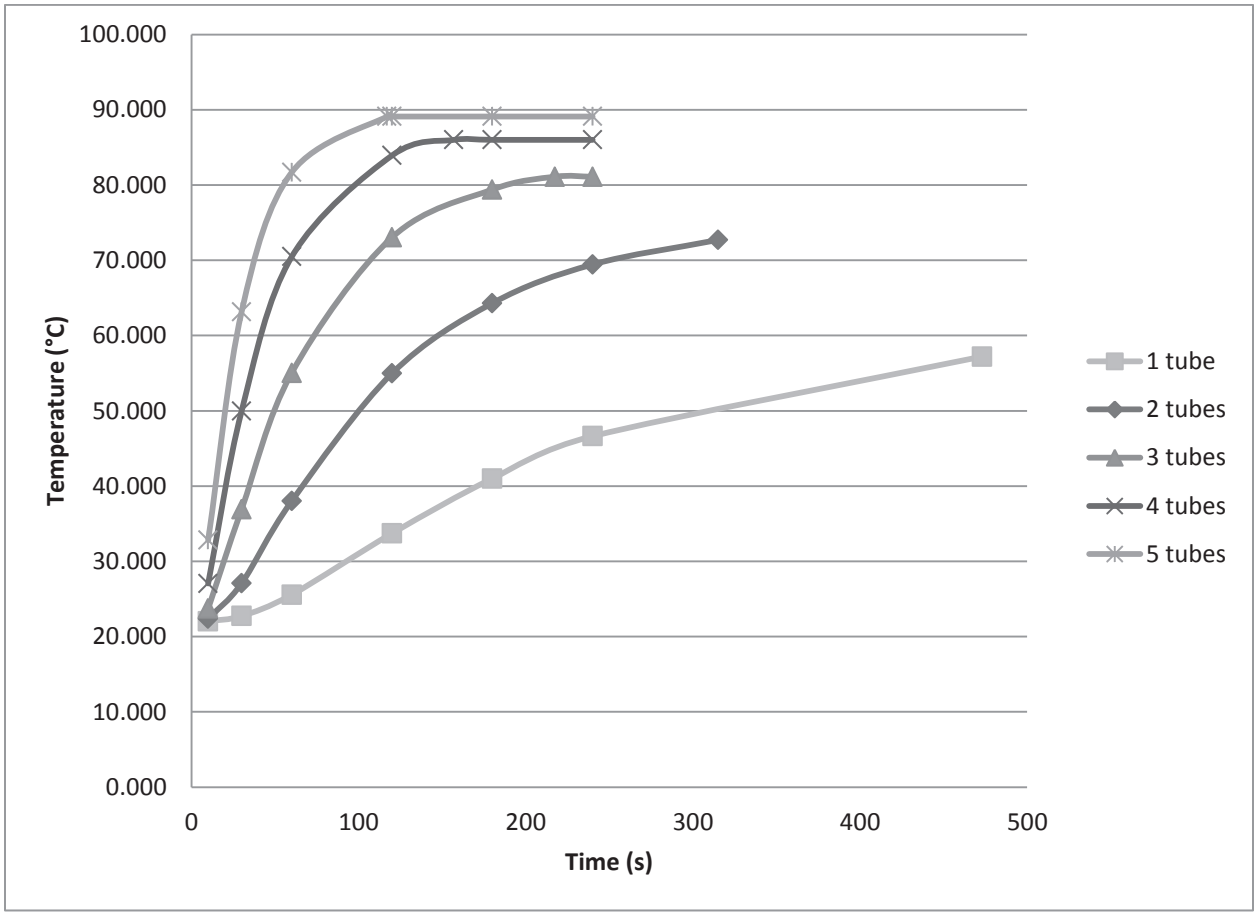

Figure 6-7. Minimum Temperature in SMP based on time.

The steady state temperature of each case as determined by the numerical calculation is shown in Table 6-2. This indicates that for a timely activation of the SMC,

more thermal delivery positions are needed. In areas where weight is concerned, potentially SMA tubes could be replaced with highly flexible tubing or grooves in the SMP to allow the thermal fluid to be more evenly spaced once enough SMA tubes are present to achieve the desired actuation.

Table 6-2. Time and temperature to reach steady state in the SMC.

	1 tube	2 tube	3 tube	4 tube	5 tube
Time to SS (in sec)	473 s	315 s	217.5 s	157 s	117 s
Temperature at SS (°C)	57.2	72.7	81.1	86.0	89.1

The temperature distribution found for each case was then used to calculate the deflection of the composite as a cantilever beam. The temperature distributions are provided in the appendix for selected temperatures along with the numerical 'A' matrix for each case (A is the matrix of coefficients of the nodal temperatures at each time-step). Table 6-3 compiles a few of the deflections using the temperature distributions found by the numerical analysis. The results show that increasing the number of tubes (and consequently the $V_{f,SMA}$) in the SMC, the SMC yields a larger deflection. It is interesting noting that the composite appears to reach a plateau value of deflection at approximately 12.5 mm, when adding a volume fraction of SMA above 2%. However, higher volume fractions of SMA in the composite significantly decreases the time needed for the system to reach its full activation.

Table 6-3. Deflection as a function of time (in mm).

Time (s)	1 tube (0.65% $V_{f,SMA}$)	2 tubes (1.3% $V_{f,SMA}$)	3 tubes (2% $V_{f,SMA}$)	4 tubes (2.65% $V_{f,SMA}$)	5 tubes (3.3% $V_{f,SMA}$)
0	1.054	1.369	1.610	1.800	1.954
30	1.753	2.591	3.893	5.890	10.085
120	2.685	6.872	11.933	12.513	12.553
180	3.220	9.543	12.367	12.538	12.553
314.75	5.241	11.788	12.400	12.538	12.553
417	6.654	11.788	12.400	12.538	12.553

6.3 FEA Results

The FEA results will be presented for the SMA deflection achieved based on the temperature and the experimental force recorded experimentally. The deflection at the end of the SMA tube will be compared to that observed at the end of the SMA experimentally. Results for the SMC from the FEA are the thermal temperature distributions through the SMC and the mechanical deflections at the end of the composite.

6.3.1 FEA Results: SMA

The SMA during heating and cooling was found to have a very short transient period of approximately 1-2 seconds in the FEA analysis, once the working fluid reached a uniform temperature (see Figure 6-7). This short transient period and uniformity allows for the approximation in future mechanical modeling by matching the inner surface temperature of the SMP.

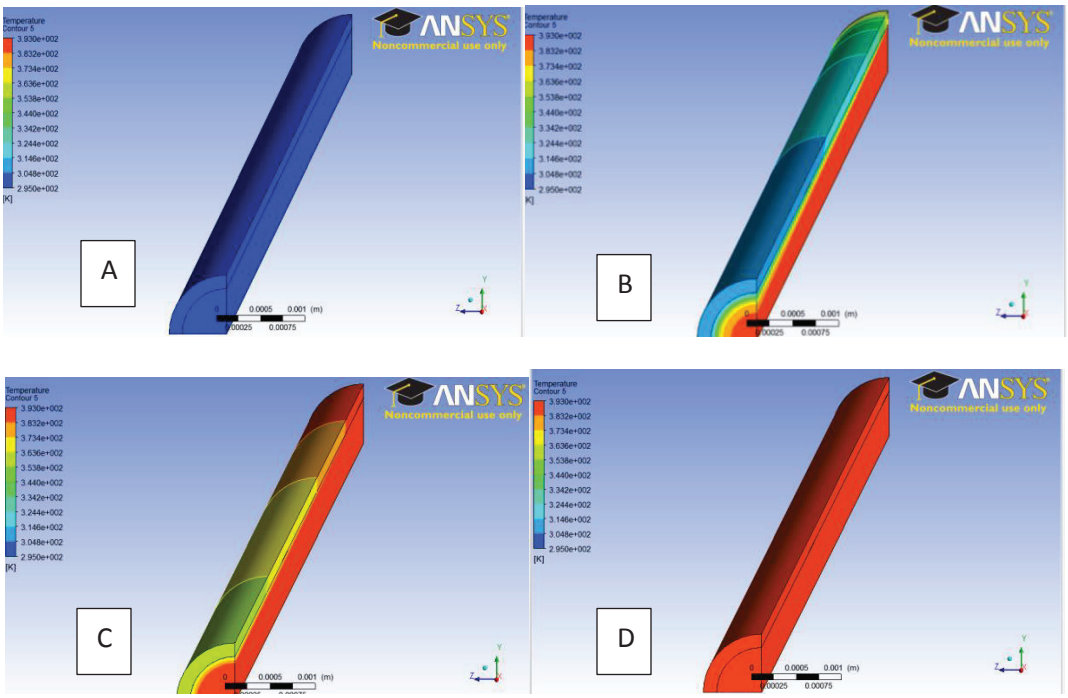

Figure 6-8. SMA Thermal Results from FEA a) initial temperature, uniform profile b) t= 0.1 s, fluid thermal profile nearly developed, transient behavior along length c) t=1s, SMA temperature has no difference through its thickness, transient behavior on length d) after t=1s, uniform temperature, similar to that recorded by the fluid source.

Once the thermal distribution through the SMA was found to be negligible the deflection of the composite was then calculated at the end of the SMA using the experimentally recovered forces on the SMA. Figure 6-9 shows the out of plane deflection of the SMA as a function of temperature. Here, 60.36 of deflection was predicted in the SMA.

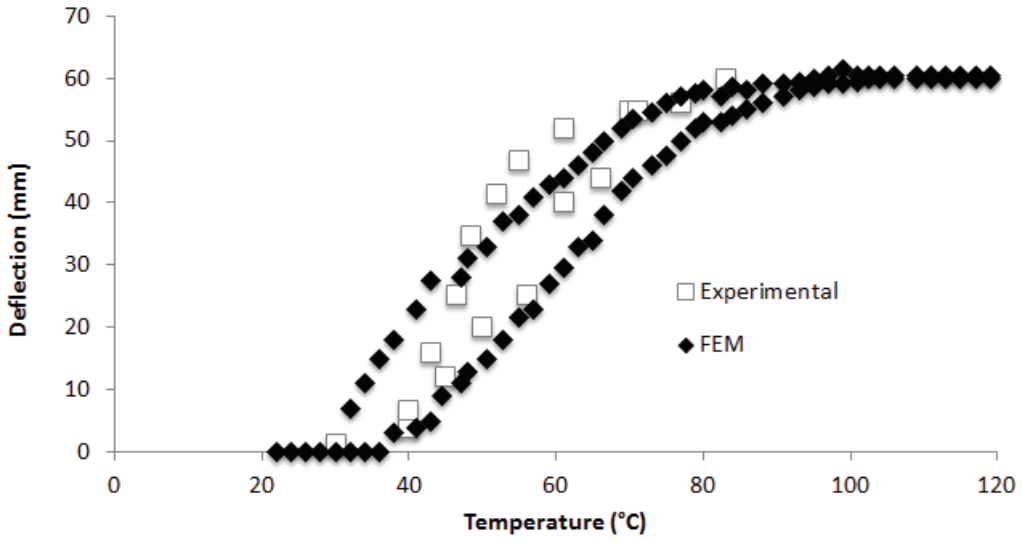

Figure 6-9. FEA predicted deflection at end of SMA through heating and cooling cycle. [48]

6.3.2 FEA results: SMC

The thermal results on the SMC were also modeled, for predicting the temperature distribution through the SMC. The thermal prediction was subsequently used in the mechanical analysis of the SMC. These results are presented in figure 6-10. Here, the temperature predicted on the SMC at 240s (steady state time, same as experiment) was 56°C and 66°C for 2 tube ($V_{f,SMA}$=1.3%) and 3 tube ($V_{f,SMA}$=2%) tube cases, respectively.

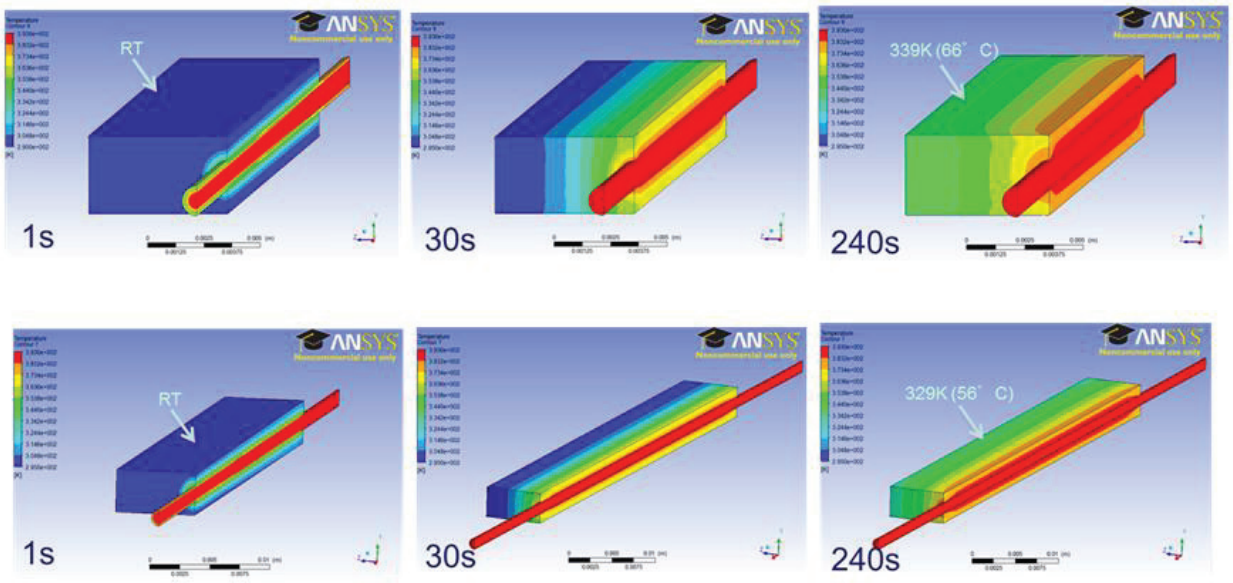

Figure 6-10. Transient FEA thermal results. (Top) 3 tubes (2% $V_{f,SMA}$) , temperature on the edge at 240s: 66°C (Bottom) 2 tubes (2% $V_{f,SMA}$), minimum temperature of 56°C, at 240s.

It is worth mentioning that the temperature predicted by the FEA seems to match those recorded during the experimental work. As previously mentioned, the thermal results were then imported into the mechanical model for predicting the deflection of the composite. The deflections of the SMC, at the end of the SMP, for the 2 cases (two and three tubes) are tabulated in Table 6-4.

Table 6-4. FEA Predicted deflection of the SMC located at the end of the SMP.

case	Deflection (mm)
2 tubes	10.006
3 tubes	16.390

Figure 6-10 shows the experimental and predicted profile of the SMC as a function of temperature. It can be observed the amount of deviation between the FEA prediction and the experimental profile.

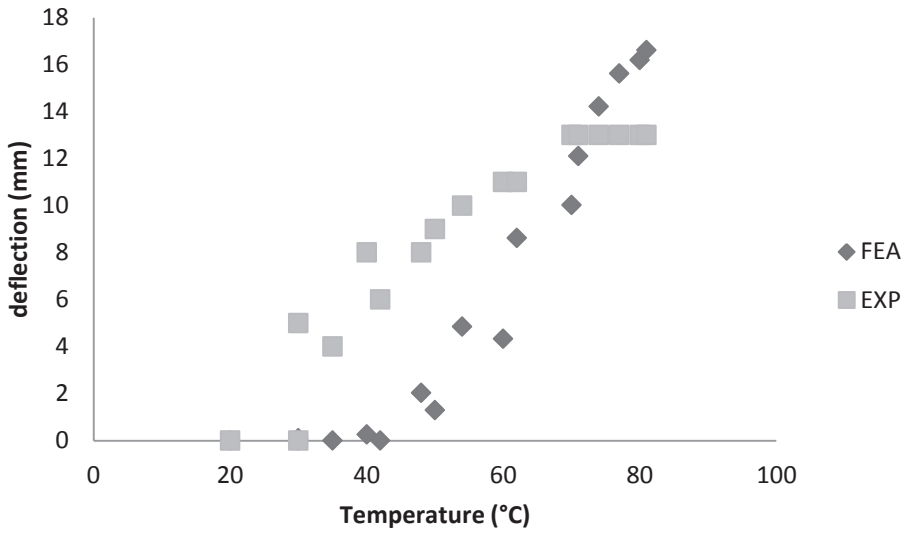

Figure 6-11. Deviation of FEA from Experimental Results. Shown for 2% $V_{f,SMA}$ (3 tubes)

6.4 Discussion

A comparison of theoretical, FEA and experimental results shows that the FEA results proved to be more reliable then the numerical method. Here, a similar percentage of error has been observed between the FEA modeling and the experimental deflection. This discrepancy could be associated to the application of the experimental clamp applied as a fixed boundary condition on the end of the SMP in the FEA. Which, in the experiment it appeared to have restricted some deflection of the SMP. The reality is somewhere off this idealized condition. Thermally, the FEA has less than 5% error from the experiment. A full comparison of the deflections and temperatures between the theoretical modeling, the FEA and the Experimental work is shown in Table 6-5.

Table 6-5. Comparison of results.

		SMA tube	2 tubes	3 tubes
experimental	SMA end δ	60	x	x
	SMC δ at the end of SMP	x	8	13
	T min at 240 s	x	59	67
FEA	SMA end δ	60.386	x	x
	% diff	0.643	x	x
	SMC δ at the end of SMP	x	10.006	16.39
	% diff	x	25.075	26.07692308
	T min at 240 s	x	56	66
	% diff	x	-5.0847	-1.492537313
theory	SMA end δ	x	x	x
	% diff	x	x	x
	SMC δ at the end of SMP	x	11.74	12.4
	% diff	x	46.75	-4.615384615
	T min at 240 s	x	69	80
	% diff	x	16.949	19.40298507

From the table, it can be observed that whereas the FEA yields a very accurate thermal prediction of the SMC, the analytical theory shows a closer mechanical deflection prediction. Again the clamping restriction applied to the SMC during the experimental work could certainly have reduced the deflection of the composite, resulting in a deviation from the predicted value.

7.0 Conclusions

The thermo-mechanical behavior of an adaptive Shape Memory Composite (SMC) based on an actuating Shape Memory Alloy (SMA) phase and a Shape Memory Polymer (SMP) matrix has been studied. Here, an initial study showed that embedding a volume fraction of the SMA phase above 1% in the SMP results in a SMC fully controlled by the SMA system. The activation process of the SMC has been further studied by incorporating two-way trained SMA vascular tubes into the SMP. The incorporation of the vascular system into the SMP allowed for the use of a thermal regulating fluid to transition the actuation process of the composite. Two different volume fractions of SMA were investigated, and it was observed that the composite with the highest volume fraction of SMA resulted in an adaptive system with superior thermal and mechanical performance. However, the analytical modeling showed that increasing the volume fraction of the SMA in the composite above 2% may not be beneficial, since the deflection in the SMC appears to yield a plateau value of approximately 12.5 mm.

A finite element analysis (FEA) has also been carried out to model the thermo-mechanical performance of the composite under transient and steady state conditions. It has been shown that although the thermal simulation provided by the FEA closely matches the thermal profile recorded during the experimental tests, certain degree of amendment on the loading conditions of the plain SMA is required in order to improve the predicted out-of-plane deflection of the composite. It can be lastly concluded that the present work has established a fundamental modeling platform for subsequent adaptive optimization of SMCs.

Bibliography

1. **Friend, Cliff.** Smart Materials. *Azom, A to Z of Materials.* Jun 11,2013.

2. **Boeing.** Boeing-Led Team Successfully . *http://www.boeing.com/news/releases/2004/q2/nr_040518t.html.* 18 May 2004.

3. **Humbeeck, J.V.** *Non-Medical Applications of Shape Memory Alloys.* s.l. : Elsevier Sciences S.A., 1999. PII: S0921-5093(99)00293-2.

4. *Shape morphing of aircraft wing: Status and Challenges.* **Sofla, A.Y.N et al.** 3, 2010, Materials and Design, Vol. 31, pp. 1284-1292.

5. *Shape memory micro-actuation for a gastro-intestinal intervention system.* **Dominiek Reynaerts, Jan Peirs, Hendrik Van Brussel.** Issue 2, October 12, 1999, Sensors and Actuators A: Physical, Vol. Volume 77, pp. Pages 157-166. ISSN 0924-4247, 10.1016/S0924-4247(99)0019.

6. *Shape-memory polymers.* **Lendlein., Marc Behl and Andreas.** Number 4, April 28 , 2007, Materials Today., Vol. 10.

7. *Elastic memory composite material: an enabling technology for future furlable space structures. In: 46th AIAA/ASME/ASCE/AHS/ASC structures.* **Campbell D, Lake MS.** Austin, Texas, : s.n., 18–21 April 2005. structural dynamics and materials conference, AIAA 2005-2362:1-9.

8. *Review of progress in Shape-Memory Polymers.* **Liu, C., Qin, H. and Mather, P.T.** 2007, J. Mater. Chem., pp. 1543-1558.

9. *Biodegradable, Elastic Shape-Memory Polymers for Potential Biomedical Application.* **Lendlein, A and Langer, R.** No. 5573, 2002, Science., Vol. 296, pp. 1673 - 1676.

10. *Demonstration of morphing technology through ground and wind tunnel tests.* **Love MH, Zink PS, Stroud RL, Bye DR, Rizk S, White D.** 2007. In: 48thAIAA/ASME/ASCE/AHS/ASC structures, structural dynamics, and materials conference, AIAA 2007-1729:1–12; .

11. *Structural shape sensing for variable camber wing using FBG sensors.* **Yin WL, Fu T, Liu JC, Leng JS.** San Diego, USA : s.n., 8–12 March, 2009. SPIE internationalconference on smart structures/NDE, Proceedings of the SPIE 7292 2009,72921H:1-10.

12. **Callister, William D.** *Materials Science and Engineering 7e.* York, PA : John Wiley & Sons, Inc, 2007.

13. **CRG.** Veritex. [Online] http://www.crgrp.com/technology/portfolio/veriflex.

14. *Memory Metal.* **Kauffman, G. and Mayo, I.** Oct. 1993, Chem Matters, pp. 4-7.

15. **Otsuka, K and Wayman, C.M.** *Shape Memory Metals.* New York : © Cambridge University Press , 1999.

16. **Auricchio, Ferdinando.** *One Way and Two Way Shape Memory Effect:Thermo-Mechanical Characteization of Ni-Ti wires.* s.l. : Universita degli Studi di Pavia , 2007/2008.

17. *Solid, shape recovered "bulk" Nitinol: Part I Tension–compression asymmetry.* **Anil Saigal, Matthew Fonte.** Issues 16–17, June 25, 2011, Materials Science and Engineering: A, Vol. Volume 528, pp. Pages 5536-5550. http://dx.doi.org/10.1016/j.msea.2011.03.

18. [Online] http://herkules.oulu.fi/isbn9514252217/html/x317.html.

19. [Online] http://www.continuum-dynamics.com/solution-me-sma-overview.html.

20. *Applications of SMA Bundles in Practical Concrete Structures.* **Lei Li, Qingbin Li and Fan Zhang.** 2013, Shape Memory Alloys - Processing, Characterization and Applications.

21. [Online] http://jmmedical.com/resources/211/Measuring-Transformation-Temperatures-in-Nitinol-Alloys.html.

22. *, Smart structure dynamics.* **Gaul, S. Hurlebaus & L.** Issue 2, February 2006, Mechanical Systems and Signal Processing, Vol. Volume 20, pp. Pages 255-281.

23. **Travis L. Turner, Randolph H. Cabell, Roberto J. Cano, and Richard J. Silcox.** Testing of SMA-enabled active chevron prototypes under representative flow conditions. [Online] http://ntrs.nasa.gov/archive/nasa/casi.ntrs.nasa.gov/20080014174_2008013560.pdf.

24. *"Overview of the DARPA Smart Wing Project," .* **Kudva, J.,.** 2004, Journal of Intelligent Material Systems and Structures., Vol. Vol.15, pp. 261-267. .

25. *An evaluation of 55 cobalt substituted Nitinol wire for use in orthodontics.* **Hilleman, G. F. Andreasen and T. B.** no. 6 , 1971, The Journal of the American Dental Association, Vol. vol. 82, pp. 1373–1375.

26. *Biomedical Applications of Shape Memory Alloys.* **Migliavacca, Lorenza Petrini and Francesco.** Article ID 501483, 2011, Journal of Metallurgy, Vol. vol. 2011.

27. **Lendlein, Andreas, [ed.].** *Shape Memory Polymers.* Berlin Heidelberg : Springer-Verla , 2010.

28. *Investigation of Shape Memory Polymers and Their Hybrid Composites .* **Liang, C., Rogers, C., and Malafeew, E.** No. 4, 1997, Journal of Intelligent Material Systems and Structures. , Vol. 8, pp. 380-386.

29. **Leng, Jinong and Du, Shanyi.** *Shape Memory Polymers and Multifunctional Composites.* s.l. : © CRC Press Taylor and Fracis Group., 2010.

30. *Mechanical and Curing Properties of a Styrene-based Shape Memory Polymer.* **Richard Beblo, Korey Gross, and Lisa Mauck Weiland.** May 2010, Journal of Intelligent Material Systems and Structures, pp. 677-683.

31. **Duenas, T., Bolanos, E., Murphy, E., Mal, A., Wudl., F., Wang, Y., Hahn, H., Ooi, T. and Bortolin, R.,.** *Multifunctional Self-Healing and Morphing Composites.* s.l. : NextGen Aeronautics Incorporated.

32. *Development of a polymer stent with shape memory effect as a drug delivery system.* **Wache, H. M., Tartakowska, D. J., Hentrich, A., and Wagner, M. H.** 2003, Journal of Materials Science: Materials in Medicine., Vol. 14, pp. 109-112.

33. *Rapidly Self-Expandable Polymeric Stents with a Shape-Memory Property.* **Mei-Chin Chen, Hung-Wen Tsai, Yen Chang, Wei-Yun Lai, Fwu-Long Mi, Chin-Tang Liu, Hen-Sheng Wong and Hsing-Wen Sung,.** 2007, Biomacromolecules, Vol. 8, pp. 2774-2780.

34. **Popov, Peter A.** *Constitutive Modeling of Shape Memory Alloys and Upscaling of Deformable Porous Media.* s.l. : Dissertation: Texas A&M University, May 2005.

35. *A macroscopic constitutive model for shape-memory alloys: Theory and finite-element simulations.* **P. Thamburaja, N. Nikabdullah.** 2009, Comput.Methods Appl.Mech. Engrg. , Vol. 198, pp. 1074–1086.

36. *Comparative Evaluation of Shape Memory Alloy ConstitutiveModels with Experimental Data.* **Prahlad, Harsha and Inderjit Chopra.** 383, 2001, Journal of Intelligent Material Systems and Structures, Vol. 12.

37. *Simplifications and comparisons of shape memory alloy constitutive models. .* **Brinson, L.C. and Huang, M.S.** 1996, Journal ofIntelligent Material Systems and Structures,, Vol. 7, pp. 108–114.

38. *A thermodynamic constitutive model for the shape memory materials part I. The monolithic shape memory alloys.* **Boyd, J.G. and Lagoudas, D.C.** 1998, International Journal of Plasticity, Vol. 6, pp. 805–842.

39. *Modeling and Control of a Shape Memory Alloy Actuator.* **Sushant M. Dutta, Fathi H. Ghorbel, and James B. Dabney.** Limassol, Cyprus : s.n., 2005, June 27-29. Proceedings of the 2005 IEEE International Symposium on Intelligent Control .

40. *Thernomechanical Constitutive model of shape memory Polymer.* **Tobushi, H., Okumura, K. Hayashi, S. Ito, N.** 2001, Mechanics of Materials, Vol. 33, pp. 545-554.

41. **Raucher, Scott G.** *testing and Analysis of Shape-memory Polymers for Morphing Aircraft Skin Applications. [thesis].* Pittsburgh, PA : University of Pittsburgh, 2006.

42. **Gross, Korey E.** *Mechanical Characterization of Shape Memory Polymers to Assess Candidacy as Morphing Aircraft Skin.[thesis].* Pittsburgh, PA : University of Pittsburgh, 2006.

43. *Analysis of Shape Memory Polymer-Alloy Composites: Modeling and Parametric Studies.* **Jungkyu Park, Leon M. Headings, Marcelo J. Dapino, Jeffery W. Baur, Gyaneshwar P. Tandon.** Stone Mountain, Georgia, USA : ASME 2012 Conference on Smart Materials, AdaptiveStructures and Intelligent Systems., September 19-21, 2012.

44. **Hisaaki Tobushi, Shnichi Hayashi, Yoshiki Sugimoto and Kousuke Date.** Two-Way Bending Properties of Shape Memory Composite with SMA and SMP. *Materials.* 2, 2009, Vols. pages 1180-1192.

45. **Chetan S. Jarali, S. Raja, Bjorn Kiefer.** *modeling the Effective Properties and Thermomechanical Behavior of SMA-SMP Multifuntional Composite Laminates.* wileyonlinelibrary.com : Wiley Online Library, Society of Plastics Engineers, 2011.

46. *A microvascular Method for thermal activation and deactivation of shape Memory Polymers.* **Baur, David M. Phillips and Jeffery W.** online : Journal of Intelligent Material Systems and Structures, 3 January 2013.

47. *The relationship between constituent property and bending actuation of shape memory composites.* **Pedro Cortes, A.J.W. McClung, J. Sakulich and J.W> Baur.** s.l. : Proceedings of the SPIE. Behavior and Mechanics of Multifunctional Materials and Composites., Volume: 8342, 03/2012.

48. *The morphing properties of a vascular shape memory composite.* **P Cortes, J Terzak, G Kubas, D Phillips and J W Baur.** s.l. : Smart Mater. Struct., 2014, Vols. 23, 015018 doi:10.1088/0964-1726/23/1/015018.

49. *Modeling of the bending actuation of a shape memory.* **Cortes P, Terzak J, McClung A J W and Baur J W.** s.l. : Proc. MS&T. pp 575–82, 2012.

Appendix

Table A-1. Numerical matrix: 1 Tube

X\T	T1	T2	T3	T4	T5	T6	T7	T8	T9	T10	T11	T12	T13	T14	T15	T16
T1	0.328	0.372	0.00724	0	0	0	0	0	0	0	0	0	0	0	0	0
T2	0.0931	0.137	0	0.00724	0	0	0	0	0	0	0	0	0	0	0	0
T3	0.486	0	0.799	0.372	0	0	0.00264	0	0	0	0	0	0	0	0	0
T4	0	0.486	0.0931	0.608	0	0	0	0.00264	0	0	0	0	0	0	0	0
T5	0	0	0	0	0.509	0.0744	0	0	0.00264	0	0	0	0	0	0	0
T6	0	0	0	0	0.486	0.846	0.0931	0	0	0.00264	0	0	0	0	0	0
T7	0	0	0.00724	0	0	0.0744	0.808	0.372	0	0	0.00264	0	0	0	0	0
T8	0	0	0	0.00724	0	0	0.0931	0.618	0	0	0	0.00264	0	0	0	0
T9	0	0	0	0	0.00264	0	0	0	0.509	0.0744	0	0	0.0106	0	0	0
T10	0	0	0	0	0	0.00264	0	0	0.486	0.846	0.093	0	0	0.0106	0	0
T11	0	0	0	0	0	0	0.00264	0	0	0.0744	0.808	0.372	0	0	0.0106	0
T12	0	0	0	0	0	0	0	0.00264	0	0	0.0931	0.618	0	0	0	0.0106
T13	0	0	0	0	0	0	0	0	0.00264	0	0	0	0.503	0.0744	0	0
T14	0	0	0	0	0	0	0	0	0	0.00264	0	0	0.486	0.840	0.093	0
T15	0	0	0	0	0	0	0	0	0	0	0.00264	0	0	0.0744	0.802	0.372
T16	0	0	0	0	0	0	0	0	0	0	0	0.00264	0	0	0.093	0.612
Tsma	0.0931	0	0.0931	0	0.00264	0.00264	0	0	0	0	0	0	0	0	0	0
T∞	0	0.0046	0	0.0046	0	0	0	0.00460	0	0	0	0.00460	0.0008	0.0008	0.0008	0.00538

Table A-2. Selected temperatures for Thermal Distribution: 1 tube

	T1	T2	T3	T4	T5	T6	T7	T8	T9	T10	T11	T12	T13	T14	T15	T16
0	22.000	22.000	22.000	22.000	22.000	22.000	22.000	22.000	22.000	22.000	22.000	22.000	22.000	22.000	22.000	22.000
0.25	29.263	22.000	29.263	22.000	22.206	22.206	22.000	22.000	22.000	22.000	22.000	22.000	22.000	22.000	22.000	22.000
5	80.525	75.585	79.862	74.901	25.265	25.186	24.625	24.453	22.074	22.072	22.060	22.056	22.004	22.004	22.004	22.003
15	93.370	91.279	92.601	90.454	31.372	31.345	31.140	31.002	22.648	22.647	22.640	22.632	22.113	22.113	22.112	22.110
30	94.440	92.574	93.751	91.834	38.956	38.927	38.707	38.494	24.319	24.317	24.299	24.273	22.743	22.743	22.738	22.729
60	95.241	93.536	94.666	92.919	49.041	49.006	48.737	48.418	28.940	28.933	28.886	28.809	25.631	25.628	25.604	25.564
120	96.064	94.524	95.610	94.037	59.628	59.586	59.267	58.835	38.515	38.500	38.391	38.209	33.900	33.890	33.812	33.681
180	96.501	95.049	96.111	94.631	65.350	65.305	64.958	64.465	46.205	46.184	46.025	45.758	41.403	41.386	41.260	41.046
240	96.784	95.389	96.437	95.017	69.090	69.042	68.677	68.145	51.898	51.872	51.676	51.346	47.127	47.105	46.941	46.664
317	97.021	95.674	96.710	95.340	72.225	72.175	71.794	71.229	56.854	56.824	56.595	56.211	52.151	52.125	51.928	51.596
473	97.289	95.995	97.018	95.704	75.767	75.715	75.317	74.714	62.517	62.482	62.217	61.770	57.906	57.875	57.640	57.245

Table A-3. Numerical matrix: 2 Tubes

X\T	T1	T2	T3	T4	T5	T6	T7	T8	T9	T10	T11	T12	T13	T14	T15	T16
T1	0.328	0.372	0.01456	0	0	0	0	0	0	0	0	0	0	0	0	0
T2	0.0931	0.137	0	0.01456	0	0	0	0	0	0	0	0	0	0	0	0
T3	0.486	0	0.785	0.372	0	0	0.00638	0	0	0	0	0	0	0	0	0
T4	0	0.486	0.0931	0.594	0	0	0	0.00638	0	0	0	0	0	0	0	0
T5	0	0	0	0	0.501	0.0744	0	0	0.00638	0	0	0	0	0	0	0
T6	0	0	0	0	0.486	0.839	0.0931	0	0	0.00638	0	0	0	0	0	0
T7	0	0	0.01456	0	0	0.0744	0.801	0.372	0	0	0.00638	0	0	0	0	0
T8	0	0	0	0.01456	0	0	0.0931	0.610	0	0	0	0.00638	0	0	0	0
T9	0	0	0	0	0.00638	0	0	0	0.501	0.0744	0	0	0.0255	0	0	0
T10	0	0	0	0	0	0.00638	0	0	0.486	0.839	0.093	0	0	0.0255	0	0
T11	0	0	0	0	0	0	0.00638	0	0	0.0744	0.801	0.372	0	0	0.0255	0
T12	0	0	0	0	0	0	0	0.00638	0	0	0.0931	0.610	0	0	0	0.0255
T13	0	0	0	0	0	0	0	0	0.00638	0	0	0	0.487	0.0744	0	0
T14	0	0	0	0	0	0	0	0	0	0.00638	0	0	0.486	0.825	0.093	0
T15	0	0	0	0	0	0	0	0	0	0	0.00638	0	0	0.0744	0.787	0.372
T16	0	0	0	0	0	0	0	0	0	0	0	0.00638	0	0	0.093	0.596
Tsma	0.0931	0	0.0931	0	0.00638	0.00638	0	0	0	0	0	0	0	0	0	0
T∞	0	0.0046	0	0.0046	0	0	0	0.00460	0	0	0	0.00460	0.0012	0.0012	0.0012	0.00581

Table A-4. Selected temperatures for Thermal Distribution: 2 tubes

	T1	T2	T3	T4	T5	T6	T7	T8	T9	T10	T11	T12	T13	T14	T15	T16
0	22.000	22.000	22.000	22.000	22.000	22.000	22.000	22.000	22.000	22.000	22.000	22.000	22.000	22.000	22.000	22.000
0.25	29.263	22.000	29.263	22.000	22.498	22.498	22.000	22.000	22.000	22.000	22.000	22.000	22.000	22.000	22.000	22.000
5	78.584	73.322	77.395	72.103	29.393	29.207	27.860	27.456	22.398	22.387	22.322	22.301	22.054	22.053	22.044	22.041
15	90.270	87.571	89.050	86.276	40.750	40.670	40.066	39.743	24.962	24.956	24.912	24.874	23.083	23.081	23.069	23.056
30	92.265	89.972	91.266	88.911	51.766	51.693	51.136	50.721	30.860	30.850	30.776	30.674	27.179	27.174	27.137	27.080
60	93.993	92.046	93.235	91.241	63.362	63.292	62.748	62.227	42.907	42.887	42.738	42.505	38.308	38.293	38.185	38.005
120	95.603	93.976	95.081	93.423	74.672	74.602	74.067	73.440	59.770	59.736	59.480	59.062	55.539	55.510	55.290	54.920
180	96.423	94.961	96.023	94.536	80.497	80.428	79.896	79.215	69.037	68.995	68.681	68.162	65.148	65.111	64.828	64.352
240	96.867	95.492	96.533	95.138	83.648	83.579	83.048	82.339	74.064	74.018	73.673	73.098	70.364	70.322	70.006	69.473
317	97.147	95.829	96.855	95.518	85.638	85.569	85.040	84.312	77.240	77.192	76.826	76.216	73.660	73.615	73.277	72.708
473	97.343	96.063	97.079	95.784	87.027	86.958	86.430	85.689	79.457	79.407	79.027	78.393	75.960	75.913	75.560	74.966

Table A-5. Numerical matrix: 3 Tubes

X\T	T1	T2	T3	T4	T5	T6	T7	T8	T9	T10	T11	T12	T13	T14	T15	T16
T1	0.328	0.372	0.02328	0	0	0	0	0	0	0	0	0	0	0	0	0
T2	0.0931	0.137	0	0.02328	0	0	0	0	0	0	0	0	0	0	0	0
T3	0.486	0	0.767	0.372	0	0	0.01221	0	0	0	0	0	0	0	0	0
T4	0	0.486	0.0931	0.576	0	0	0	0.01221	0	0	0	0	0	0	0	0
T5	0	0	0	0	0.490	0.0744	0	0	0.01221	0	0	0	0	0	0	0
T6	0	0	0	0	0.486	0.827	0.0931	0	0	0.01221	0	0	0	0	0	0
T7	0	0	0.02328	0	0	0.0744	0.789	0.372	0	0	0.01221	0	0	0	0	0
T8	0	0	0	0.02328	0	0	0.0931	0.599	0	0	0	0.01221	0	0	0	0
T9	0	0	0	0	0.01221	0	0	0	0.490	0.0744	0	0	0.0488	0	0	0
T10	0	0	0	0	0	0.01221	0	0	0.486	0.827	0.093	0	0	0.0488	0	0
T11	0	0	0	0	0	0	0.01221	0	0	0.0744	0.789	0.372	0	0	0.0488	0
T12	0	0	0	0	0	0	0	0.01221	0	0	0.0931	0.599	0	0	0	0.0488
T13	0	0	0	0	0	0	0	0	0.01221	0	0	0	0.464	0.0744	0	0
T14	0	0	0	0	0	0	0	0	0	0.01221	0	0	0.486	0.801	0.093	0
T15	0	0	0	0	0	0	0	0	0	0	0.01221	0	0	0.0744	0.763	0.372
T16	0	0	0	0	0	0	0	0	0	0	0	0.01221	0	0	0.093	0.572
Tsma	0.0931	0	0.0931	0	0.01221	0.01221	0	0	0	0	0	0	0	0	0	0
T∞	0	0.0046	0	0.0046	0	0	0	0.00460	0	0	0	0.00460	0.0017	0.0017	0.0017	0.00627

Table A-6. Selected temperatures for Thermal Distribution: 3 tubes

	T1	T2	T3	T4	T5	T6	T7	T8	T9	T10	T11	T12	T13	T14	T15	T16
0	22.000	22.000	22.000	22.000	22.000	22.000	22.000	22.000	22.000	22.000	22.000	22.000	22.000	22.000	22.000	22.000
0.25	29.263	22.000	29.263	22.000	22.952	22.952	22.000	22.000	22.000	22.000	22.000	22.000	22.000	22.000	22.000	22.000
5	76.751	71.187	75.108	69.517	34.871	34.536	32.041	31.308	23.289	23.253	23.035	22.968	22.315	22.306	22.253	22.236
15	88.235	85.145	86.746	83.583	50.239	50.081	48.857	48.298	29.887	29.865	29.723	29.613	26.463	26.454	26.398	26.342
30	91.244	88.760	90.110	87.569	62.302	62.173	61.171	60.551	41.644	41.617	41.427	41.196	37.209	37.193	37.077	36.905
60	93.900	91.942	93.138	91.142	74.626	74.518	73.678	72.980	59.615	59.576	59.290	58.865	55.673	55.642	55.412	55.038
120	96.217	94.718	95.791	94.271	85.671	85.580	84.878	84.109	77.090	77.038	76.655	76.043	73.965	73.919	73.574	73.000
180	97.042	95.707	96.736	95.385	89.608	89.524	88.870	88.075	83.338	83.282	82.864	82.184	80.510	80.459	80.072	79.426
240	97.337	96.060	97.073	95.783	91.015	90.933	90.297	89.493	85.570	85.513	85.083	84.379	82.849	82.795	82.394	81.723
317	97.456	96.202	97.209	95.943	91.580	91.499	90.870	90.062	86.467	86.409	85.974	85.260	83.788	83.734	83.327	82.645
473	97.498	96.252	97.257	96.001	91.782	91.701	91.075	90.266	86.788	86.730	86.293	85.576	84.124	84.070	83.661	82.975

Table A-7. Numerical matrix: 4 Tubes

X\T	T1	T2	T3	T4	T5	T6	T7	T8	T9	T10	T11	T12	T13	T14	T15	T16
T1	0.328	0.372	0.03289	0	0	0	0	0	0	0	0	0	0	0	0	0
T2	0.0931	0.137	0	0.03289	0	0	0	0	0	0	0	0	0	0	0	0
T3	0.486	0	0.748	0.372	0	0	0.02058	0	0	0	0	0	0	0	0	0
T4	0	0.486	0.0931	0.557	0	0	0	0.02058	0	0	0	0	0	0	0	0
T5	0	0	0	0	0.473	0.0744	0	0	0.02058	0	0	0	0	0	0	0
T6	0	0	0	0	0.486	0.810	0.0931	0	0	0.02058	0	0	0	0	0	0
T7	0	0	0.03289	0	0	0.0744	0.773	0.372	0	0	0.02058	0	0	0	0	0
T8	0	0	0	0.03289	0	0	0.0931	0.582	0	0	0	0.02058	0	0	0	0
T9	0	0	0	0	0.02058	0	0	0	0.473	0.0744	0	0	0.0823	0	0	0
T10	0	0	0	0	0	0.02058	0	0	0.486	0.810	0.093	0	0	0.0823	0	0
T11	0	0	0	0	0	0	0.02058	0	0	0.0744	0.773	0.372	0	0	0.0823	0
T12	0	0	0	0	0	0	0	0.02058	0	0	0.0931	0.582	0	0	0	0.0823
T13	0	0	0	0	0	0	0	0	0.02058	0	0	0	0.430	0.0744	0	0
T14	0	0	0	0	0	0	0	0	0	0.02058	0	0	0.486	0.767	0.093	0
T15	0	0	0	0	0	0	0	0	0	0	0.02058	0	0	0.0744	0.729	0.372
T16	0	0	0	0	0	0	0	0	0	0	0	0.02058	0	0	0.093	0.538
Tsma	0.0931	0	0.0931	0	0.02058	0.02058	0	0	0	0	0	0	0	0	0	0
T∞	0	0.0046	0	0.0046	0	0	0	0.00460	0	0	0	0.00460	0.0022	0.0022	0.0022	0.00676

Table A-8. Selected temperatures for Thermal Distribution: 4 tubes

	T1	T2	T3	T4	T5	T6	T7	T8	T9	T10	T11	T12	T13	T14	T15	T16
0	22.000	22.000	22.000	22.000	22.000	22.000	22.000	22.000	22.000	22.000	22.000	22.000	22.000	22.000	22.000	22.000
0.25	29.263	22.000	29.263	22.000	23.605	23.605	22.000	22.000	22.000	22.000	22.000	22.000	22.000	22.000	22.000	22.000
5	75.285	69.482	73.328	67.511	41.177	40.660	36.714	35.576	25.118	25.031	24.489	24.322	23.168	23.135	22.938	22.876
15	87.250	83.980	85.653	82.323	58.655	58.406	56.433	55.619	37.471	37.420	37.084	36.854	33.252	33.226	33.056	32.907
30	91.218	88.738	90.103	87.580	71.307	71.123	69.657	68.845	54.544	54.492	54.131	53.735	50.569	50.534	50.290	49.960
60	94.789	93.012	94.170	92.370	83.982	83.850	82.803	81.969	74.394	74.335	73.911	73.313	71.430	71.382	71.027	70.474
120	97.083	95.758	96.785	95.450	92.180	92.081	91.302	90.454	87.357	87.294	86.827	86.097	85.083	85.025	84.598	83.899
180	97.546	96.313	97.314	96.073	93.836	93.745	93.019	92.168	89.977	89.913	89.437	88.680	87.841	87.782	87.340	86.612
240	97.640	96.425	97.421	96.198	94.171	94.081	93.366	92.514	90.506	90.442	89.964	89.202	88.399	88.339	87.894	87.160
317	97.660	96.449	97.444	96.226	94.244	94.154	93.442	92.590	90.622	90.558	90.080	89.316	88.521	88.461	88.016	87.280
473	97.664	96.453	97.448	96.230	94.256	94.166	93.454	92.602	90.640	90.576	90.098	89.334	88.540	88.480	88.034	87.298

Table A-9. Numerical matrix: 5 Tubes

X\T	T1	T2	T3	T4	T5	T6	T7	T8	T9	T10	T11	T12	T13	T14	T15	T16
T1	0.328	0.372	0.04304	0	0	0	0	0	0	0	0	0	0	0	0	0
T2	0.0931	0.137	0	0.04304	0	0	0	0	0	0	0	0	0	0	0	0
T3	0.486	0	0.728	0.372	0	0	0.03208	0	0	0	0	0	0	0	0	0
T4	0	0.486	0.0931	0.537	0	0	0	0.03208	0	0	0	0	0	0	0	0
T5	0	0	0	0	0.450	0.0744	0	0	0.03208	0	0	0	0	0	0	0
T6	0	0	0	0	0.486	0.787	0.0931	0	0	0.03208	0	0	0	0	0	0
T7	0	0	0.04304	0	0	0.0744	0.750	0.372	0	0	0.03208	0	0	0	0	0
T8	0	0	0	0.04304	0	0	0.0931	0.559	0	0	0	0.03208	0	0	0	0
T9	0	0	0	0	0.03208	0	0	0	0.450	0.0744	0	0	0.1283	0	0	0
T10	0	0	0	0	0	0.03208	0	0	0.486	0.787	0.093	0	0	0.1283	0	0
T11	0	0	0	0	0	0	0.03208	0	0	0.0744	0.750	0.372	0	0	0.1283	0
T12	0	0	0	0	0	0	0	0.03208	0	0	0.0931	0.559	0	0	0	0.1283
T13	0	0	0	0	0	0	0	0	0.03208	0	0	0	0.383	0.0744	0	0
T14	0	0	0	0	0	0	0	0	0	0.03208	0	0	0.486	0.720	0.093	0
T15	0	0	0	0	0	0	0	0	0	0	0.03208	0	0	0.0744	0.683	0.372
T16	0	0	0	0	0	0	0	0	0	0	0	0.03208	0	0	0.093	0.492
Tsma	0.0931	0	0.0931	0	0.03208	0.03208	0	0	0	0	0	0	0	0	0	0
T∞	0	0.0046	0	0.0046	0	0	0	0.00460	0	0	0	0.00460	0.0027	0.0027	0.0027	0.00730

Table A-10. Selected temperatures for Thermal Distribution: 5 tubes

	T1	T2	T3	T4	T5	T6	T7	T8	T9	T10	T11	T12	T13	T14	T15	T16
0	22.000	22.000	22.000	22.000	22.000	22.000	22.000	22.000	22.000	22.000	22.000	22.000	22.000	22.000	22.000	22.000
0.25	29.263	22.000	29.263	22.000	24.502	24.502	22.000	22.000	22.000	22.000	22.000	22.000	22.000	22.000	22.000	22.000
5	74.283	68.318	72.155	66.197	47.713	47.004	41.410	39.825	28.209	28.033	26.925	26.585	25.185	25.095	24.553	24.384
15	87.079	83.785	85.499	82.163	66.152	65.815	63.074	62.012	47.006	46.909	46.271	45.876	42.860	42.800	42.418	42.125
30	92.073	89.766	91.112	88.779	79.488	79.266	77.452	76.483	67.288	67.207	66.642	66.076	64.120	64.061	63.650	63.151
60	96.049	94.523	95.619	94.082	90.732	90.596	89.493	88.584	85.047	84.973	84.441	83.717	82.889	82.827	82.369	81.683
120	97.657	96.447	97.443	96.228	95.285	95.185	94.369	93.483	92.244	92.174	91.655	90.866	90.498	90.433	89.957	89.194
180	97.811	96.631	97.618	96.434	95.721	95.624	94.836	93.953	92.933	92.863	92.346	91.550	91.226	91.162	90.683	89.914
240	97.825	96.649	97.634	96.453	95.763	95.666	94.881	93.998	92.999	92.929	92.412	91.616	91.296	91.231	90.753	89.983
317	97.827	96.650	97.636	96.455	95.767	95.670	94.885	94.002	93.006	92.936	92.418	91.623	91.303	91.238	90.760	89.989
473	97.827	96.650	97.636	96.455	95.768	95.671	94.885	94.002	93.006	92.936	92.419	91.623	91.303	91.239	90.760	89.990